Mechanics of Materials 199 (2024) 105144

Contents lists available at ScienceDirect

Mechanics of Materials

journal homepage: www.elsevier.com/locate/mecmat

Research paper

Experimental investigation and micromechanical analysis of glass fiber reinforced polyamide 6

Marie-Christine Reuvers [a,*], Christopher Dannenberg [a], Sameer Kulkarni [b], Klara Loos [b], Michael Johlitz [b], Alexander Lion [b], Stefanie Reese [a,c], Tim Brepols [a]

[a] Institute of Applied Mechanics, RWTH Aachen University, Mies-van-der-Rohe-Str. 1, 52074 Aachen, Germany
[b] Institute of Mechanics, University of the German Federal Armed Forces Munich, Werner-Heisenberg-Weg 39, 85577 Neubiberg, Germany
[c] University of Siegen, Adolf-Reichwein-Str. 2a, 57076 Siegen, Germany

ARTICLE INFO

Keywords:
Polyamide 6
Glass fiber reinforced polymer (GFRP)
Experimental testing
Thermomechanical coupling
Computational micromechanics

ABSTRACT

Achieving process stability in the thermoforming of fiber reinforced polymer materials (FRPs) for aerospace or automotive manufacturing is usually associated with a costly trial-and-error process, where experimental boundary conditions and other influencing factors, such as, for example, material composition, need to be adjusted over time. This is especially true when material phenomena on the microlevel, such as the crystallization kinetics of the polymer matrix or resulting stresses from temperature gradients, are the cause of the process instability. To reduce the experimental effort and reliably predict the material behavior during thermoforming, finite element simulation tools on multiple scales are a useful solution. Hereby, incorporating micromechanical phenomena into the model approaches is crucial for an accurate prediction by further reducing the deviation between simulation and experiment, in particular with regard to the underlying nonlinear material behavior. In this work, unit cell simulations on the microscale of a unidirectional glass fiber reinforced polymer (UD GFRP) are conducted to predict effective thermomechanical properties of a single material ply and ascertain the effect of individual ply constituents on the homogenized material behavior. The polymeric matrix material model used was identified in a prior publication with experimental data at various temperatures for polyamide 6 blends with varying degrees of crystallinities. Various randomization methods are tested to generate the unit cells and replicate the composites' random fiber distribution, with a focus on process automation. The simulative results are successfully compared to an experimental study on glass fiber reinforced polyamide 6 tested at various temperatures, demonstrating the potential of the approach to reduce both time and cost required for material characterization. Finally, the unit cells are used to generate a database to predict untested load cases that will be used in future work to characterize a homogenized macroscopic material model.

1. Introduction

Nowadays, fiber reinforced polymers (FRPs) are extensively used in applications where good thermomechanical properties are required in combination with weight savings and cost-effective mass production. These composite materials are manufactured with a broad variety of constituents and more and more often recyclability and reusability are key factors for the design process. However, despite their popularity in industry and cross-sector usage the accurate prediction and performance of forming processes such as e.g. thermoforming often remains a process of trial and error. In many cases, the final product exhibits unwanted deformations after forming that need to be eradicated with time-consuming and costly experiments until all process parameters are dialed in. Especially, the complex behavior of the polymeric matrix material undergoing a second order phase change around the glass transition regime is difficult to predict and still an ongoing research topic on its own today (see e.g. Hadipeykani et al., 2020; Xie et al., 2020). In the case of a semi-crystalline polymer matrix, the recrystallization during cooling is another process that is crucial not only for the resulting material performance but also for the interplay between fiber and matrix at their interface is a challenging factor.

Experimentally obtained results for one specific FRP system cannot be extrapolated to other configurations with different fiber volume

* Corresponding author.
E-mail addresses: marie.reuvers@ifam.rwth-aachen.de (M.-C. Reuvers), christopher.dannenberg@rwth-aachen.de (C. Dannenberg), sameer.kulkarni@unibw.de (S. Kulkarni), klara.loos@unibw.de (K. Loos), michael.johlitz@unibw.de (M. Johlitz), alexander.lion@unibw.de (A. Lion), stefanie.reese@uni-siegen.de (S. Reese), tim.brepols@rwth-aachen.de (T. Brepols).

https://doi.org/10.1016/j.mechmat.2024.105144
Received 10 June 2024; Received in revised form 18 August 2024; Accepted 2 September 2024
Available online 3 September 2024

fractions or constituent properties, such as for example the matrix degree of crystallinity (DOC). Therefore, to characterize material model formulations for various material systems, experiments need to be repeated, leading to a massive investment for model identification and verification (see e.g. Naya et al., 2017). To consider micromechanical effects, which are often critical to understanding material failure during a forming process, additional experiments are required to account for the individual constituents, even though the material behavior of the composite may already be known. In addition, the simultaneous consideration of an increasing number of boundary conditions and material phenomena, such as temperature, moisture content, environmental factors, time-dependent material behavior, underlying morphology, kinematic rotation of the fibers during forming, or damage, dramatically increases the number of experiments required. Consequently, computational approaches are needed to reduce the set of experiments without compromising on data and at the same time increasing the reusability for different material systems through a universal approach.

To investigate micromechanical effects and further incorporate them on the macrolevel without conducting new experiments, several computational approaches exist (Geers et al., 2010). Classical, fully coupled modeling schemes such as FE^2 (see e.g. Feyel and Chaboche, 2000; Schröder, 2014; Raju et al., 2021) or FE-FFT (see e.g. Spahn et al., 2014; Schneider, 2021; Gierden et al., 2022) pass the macroscopic deformation to the microscale in every Gauss point, where an additional boundary value problem is solved on a unit cell. The resulting stress state as well as the tangent operator are transferred back to the macroscale as volume averages over the microscopic domain to achieve a global solution. Herein, several contributions also address multiphysical problems such as, for example, thermomechanical coupling (see e.g. Özdemir et al., 2008; Temizer and Wriggers, 2011; Li et al., 2019; Wicht et al., 2021; Schmidt et al., 2023) or damage (see e.g. Spahn et al., 2014). These approaches are known to predict the macroscopic material behavior with a high degree of accuracy, provided that there is sufficient separation of scales. However, the computational cost is usually very high (cf. Geers et al., 2010). Another method to achieve the homogenized macroscopic solution are uncoupled multiscale approaches, where numerical simulations on a representative part of the composite microstructure are used as virtual experiments to generate input data for the characterization of the material models on the macroscale (see e.g. Naya et al., 2017). Thereby, the homogenized microscopic response in terms of e.g. effective material properties is in close agreement with experimental data on the higher scale given an appropriate choice of the microscopic domain. In addition to the lower computational cost associated with the uncoupled solution, complex experimental stress or strain conditions such as multiaxial loadings can be reproduced without the corresponding experimental effort. Furthermore, varying boundary conditions can easily be applied on the microstructure and their effect on the macroscale can be investigated in detail.

In the context of FRPs, computational micromechanics have been used intensively to study the composites failure behavior. Melro et al. (2013b), for example, developed a constitutive damage model for an epoxy matrix that was used in a micromechanical analysis with unidirectional (UD) fiber reinforcement to predict ply properties in Melro et al. (2013a). Apart from the matrix damage, the delamination between fibers and matrix at their interface was studied using cohesive zone elements. Similar investigations were conducted by Naya et al. (2017), who further incorporated a cohesive damage-friction model for fiber matrix debonding and validated the numerical results against experimental data. Interfiber/interlaminar failure prediction was studied by Hinton et al. (2004) and Daniel et al. (2009), whereas Selmi et al. (2011) used mean-field homogenization to investigate the biaxial yield as well as the plastic regime of short glass fiber reinforced polyamide. More recent publications from Poggenpohl et al. (2022b,a) focused on the development of a homogenization approach for the failure zone of carbon fiber reinforced polymers (CFRPs). The generation of statistically equivalent fiber distributions in unit cells was discussed by e.g. Vaughan and McCarthy (2010), Wang et al. (2016) and Bargmann et al. (2018), while the influence of the shape of the individual fibers on the resulting macroscopic material behavior was investigated by, for example, Herráez et al. (2016). The influence of the fiber volume content and the fiber length distribution on the elastic and thermoelastic behavior of short fiber composites were studied by Hine et al. (2002), whereas the influence of the thermal history on the interfacial properties of carbon fiber reinforced polyamide 6 composites was studied by Li et al. (2016). In terms of multiphysical micromechanical investigations, especially regarding the thermomechanical behavior of FRPs, only a few contributions are available, where, to the authors' knowledge, the influence of the DOC is not taken into account yet. Therefore, in this work, a micromechanical analysis will be conducted on glass fiber reinforced polyamide 6 repeating unit cells (RUCs) and extended to account for the effective thermal material response in order to generate a virtual data basis for the identification of a homogenized macroscopic material model. For validation purposes, an experimental study is carried out on the composite.

In contrast to existing publications, this approach employs a thermomechanically coupled matrix material formulation developed by Reuvers et al. (2024) and Kulkarni et al. (2022, 2023) in a preceding step. This formulation has been validated through extensive mechanical and thermal experimental studies conducted on polyamide 6 blends. Its applicability is demonstrated across a wide range of crystallinities and temperatures. Consequently, the authors are able to generate virtual composite data for a wide range of matrix degrees of crystallinity (DOCs) and temperatures after validating the results of the micromechanical analysis for one DOC. This approach thus leads to a significant decrease in the overall experimental effort without any compromise to the experimental findings. In other words, the presented approach allows for the generation of experimental data in a virtual manner, thereby enabling the testing of a broad variety of boundary conditions or load cases that would otherwise require an extensive amount of time if tested experimentally. Furthermore, the integration of further micromechanical phenomena related to the polymeric matrix, such as damage or moisture dependence, is straightforward. The same methodology can be applied to other semi-crystalline thermoplastic composite materials in the future.

The accompanying experimental preparation and procedure are stated in Section 2, where a direction dependent mechanical and thermal analysis is carried out. Next, in Section 3 the thermodynamically consistent, thermo-mechanically coupled material model formulation for the polyamide 6 matrix is briefly summarized. Here, the degree of crystallinity serves as a constant input variable. Visco-elastic and elasto-plastic contributions are combined together with a nonlinear kinematic hardening of Armstrong–Frederick type and a tension–compression asymmetry in yielding. In Section 4, the generation of repeating unit cells is discussed using various different randomization methods with a focus on process automation. Moreover, a statistical analysis is carried out to determine the resulting mesh and RUC size. The identification of the matrix model with experiments carried out on polyamide 6 blends in Reuvers et al. (2024) is briefly summarized in Section 5 together with an extension of the parameter range to account for the composite material. Subsequently, the numerical results are compared to experimental findings to examine the validity of the RUCs. Further mechanical and thermal numerical results enrich the data basis for the characterization of a macroscopic material model formulation. Finally, in Section 6 a conclusion is drawn, and an outlook is given.

2. Experimental investigation

2.1. Specimen preparation

The objective of the experimental investigation was to obtain engineering stress–strain data for various constant temperatures and strain

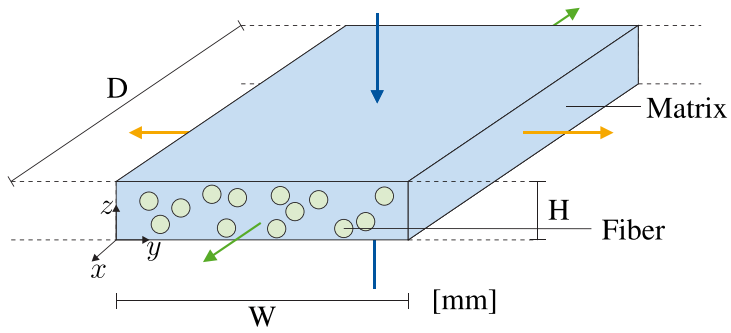

Orientation to fiber direction	Load case	Width [mm]	Depth [mm]	Height[mm]
∥	Tension	10	100	5
⊥	Tension	100	20	5
⊥	Compression	10	10	10
∥	Three-point bending	15	100	5
⊥	Three-point bending	100	15	5

Fig. 1. Schematic overview of the sample geometries and mechanical test cases.

rates in the direction of the fibers (x-direction) and perpendicular to them (y- and z-direction). Therefore, unidirectionally (UD) fiber reinforced plates were manufactured by Bond Laminates (Lanxess) as 102-RGUDm317 Tepex® dynalite sheets with 40% fiber volume content and a polyamide 6 matrix.[1] To ensure comparability with the experiments conducted to characterize the existing matrix material model (see Reuvers et al., 2024), the same PA6 granulate was used for the production of the plates. Here, randomly distributed UD roving glass fibers with a diameter of approximately 17 µm were used for UD tape production and stacked in 16 or 32 layers for manufacturing to achieve two material thicknesses of 5 and 10 mm, respectively. In the following, the 5 mm plates were used for all tension and bending tests as well as for the thermomechanical analysis (TMA) and the dynamical mechanical analysis (DMA), whereas the 10 mm plate served for compression and conduction tests. After production, the plates were cut into $100 \times 5 \times 10$ mm^3 and $100 \times 5 \times 20$ mm^3 specimens for the tension tests in fiber direction and perpendicular to it, in line with DIN EN ISO 527-5. Note here that all tests under varying fiber angle were performed with the latter specimen size as well. For the compression tests, smaller samples with $10 \times 10 \times 10$ mm^3 were needed according to DIN EN ISO 604. For the three-point bending experiments in y- and z-direction, the specimens were cut into strips of $100 \times 15 \times 5$ mm^3 in line with DIN EN ISO 14125. An overview of the sample geometries and the coordinate system that will be used throughout this work is provided in Fig. 1. For cutting, a diamond saw was utilized together with a water jet for cooling purposes, since the heat generated during sawing could potentially alter the degree of crystallinity of the polyamide 6 matrix. Afterwards, the wet specimens were stored in a *MP Dry Cabinet IV ST* (MP Elektronik Technologie, Svitávka, Czech Republic) until the moisture content obtained from an *Aquatrack* (Brabender (Anton Paar), Duisburg, Germany) measurement was less than 0.1%. Until testing, the specimens were stored in vacuum sealed aluminum bags to prevent water absorption due to the hygroscopic matrix material.

2.2. Differential scanning calorimetry

Prior to the mechanical and thermal experimental investigations, the degree of crystallinity of the composite was determined via differential scanning calorimetry (DSC) at the Polymer Service GmbH Merseburg (PSM) Germany. For this procedure, only a small fraction of material (ideally < 10 mg) is needed. However, due to the random dispersion of the glass fibers in the polyamide 6 matrix, cutting and testing a small part of a specimen does not guaranty the desired 40% fiber volume content in the probe. To overcome this problem and to achieve sample material with the correct fiber volume content, slices from four different measurement positions of a specimen were taken and subsequently ground to powder. Next, a fraction of the powder was used for the DSC analysis and afterwards burned via thermogravimetric analysis (TGA) to determine the true amount of glass fibers in the tested sample. As can be seen in Table 1, the four locations yielded similar results in the DSC analysis and the TGA confirmed that the correct amount of fibers was met when calculating the volume percentage with the fiber density. Next, the melting enthalpy ΔH_m obtained from the integrated area under the peak of the heat flow over time of the first and second heating run was corrected with the PA6 mass fraction to resemble a material with 100% PA6 content ($\Delta H_m^{100,\mathrm{PA6}}$). Together with the specific fusion enthalpy for a hypothetically 100% crystalline material ($\Delta H_0^{100} = 190$ J/g from Campoy et al. (1998)), the absolute DOC of the matrix was calculated by

$$\chi = \frac{\Delta H_m^{100,\mathrm{PA6}}}{\Delta H_0^{100}}. \tag{1}$$

The mean value for the first heating run of the four test locations was found to be $\chi \approx 0.41$. This value will be used in the following to obtain the matrix properties together with the results of the identification procedure in Reuvers et al. (2024).

Similar to Reuvers et al. (2024) for pure PA6, the glass transition temperature of the composite was around 58 °C. The authors anticipated this outcome, given that the same PA6 granulate was used for specimen production and the glass fibers behave purely amorphously.

2.3. Microscopic examination

To gain a direct insight into the materials' microstructure for the unit cell generation in Section 4, microscopic in-ply images were taken on a *Zeiss Axiophot* (Zeiss, Oberkochen, Germany) microscope with *ProgRes SpeedXT Core 5* (Jenoptik, Jena, Germany) camera at the Institute of Mechanics, University of the German Federal Armed Forces, Munich. Therefore, a small sample of the composite material was enclosed in epoxy, and further ground and polished with a *LaboSystem LaboPol-30* and *LaboForce-100* (Struers, Champigny sur Marne cedex, France)

[1] The thermal histories associated with the production of the tape and laminate are not available due to the commercial nature of the product.

Table 1
Differential scanning calorimetry (DSC) and thermogravimetric analysis (TGA): Results and average at four different measuring locations.

	Weight [mg]	Melting enthalpy [J/g]		GF content [mass-%]	Corrected melting enthalpy [J/g]		DOC [%]	
		1.HR	2. HR		1.HR	2. HR	1.HR	2. HR
M1	6.48	29.77	30.36	0.6274	79.90	81.48	42.05	42.88
M2	6.72	28.26	28.75	0.6334	77.09	78.42	40.57	41.28
M3	7.68	27.27	29.04	0.6396	75.67	80.58	39.82	42.41
M4	7.10	31.39	31.46	0.6047	79.41	79.59	41.79	41.89
Avg.	7.00	29.173	29.903	0.6263	78.015	80.017	41.06	42.11

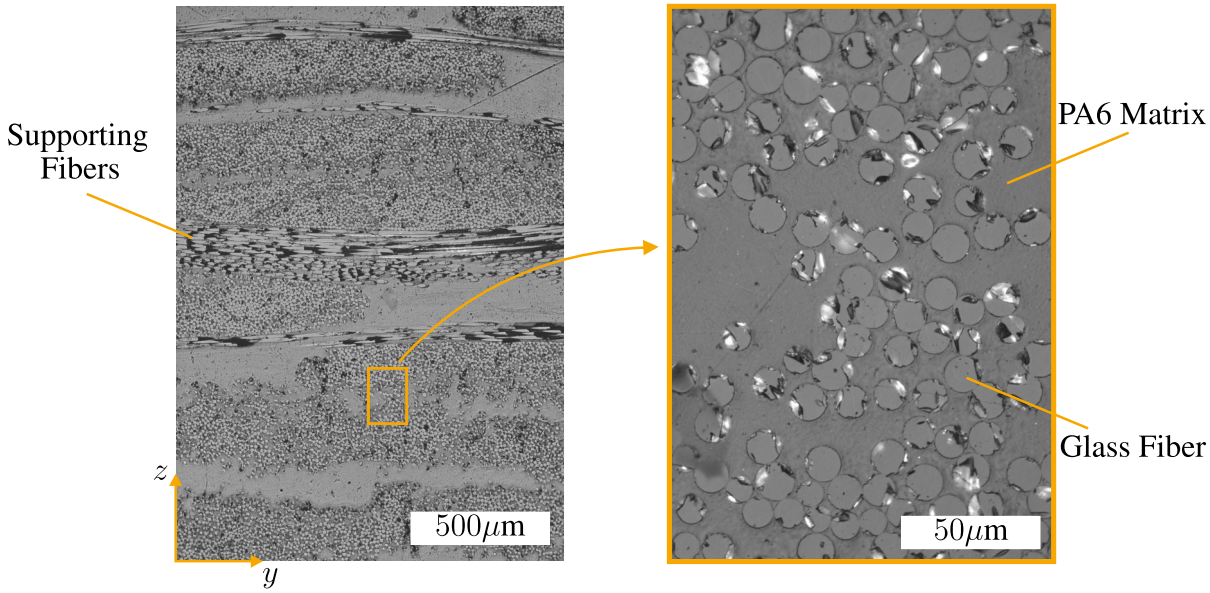

Fig. 2. Microscopic pictures showing the random fiber distribution and the layer structure of the composite.

machine until a clear image was visible under the microscope. In Fig. 2, two material sections are shown with different magnification. As indicated in the picture, the glass fibers are randomly distributed in the polyamide 6 matrix. Additionally, supporting fibers in weft direction are visible, which are necessary to ensure stability during the production process. According to the manufacturer specifications, only three percent of the total fiber volume content are supporting fibers, hence, these fibers are neglected for the unit cell generation in Section 4. Moreover, the glass fibers show a variation in cross-sectional area. To incorporate this phenomenon, further microscopic images on a range of samples would be necessary in combination with statistical investigations which is beyond the scope of this work. Therefore, the authors chose to approximate the cross section of the glass fibers as circular disks with a constant diameter of 17 μm according to the manufacturer. Interestingly enough, in the left image in Fig. 2a laminate like pattern is visible, where layers consisting predominantly of matrix material separate layers including fibers.

This effect stems from the production process, where firstly prepregs are produced out of a single layer of unidirectional glassfibers coated with PA6 powder. In the next processing step, several prepreg rolls are layered and combined to a composite during an impregnation and consolidation step. Here, the PA6 powder melts under temperature and forms the matrix. The application of pressure ensures an air pocket free composite in which every fiber is surrounded by the thermoplastic matrix. In our case, 16 and 32 layers were realized for a resulting composite thickness of 5 and 10 mm, respectively. Naturally, the layered structure remains even after consolidation, resulting in areas where only matrix material is present.

2.4. Mechanical testing

2.4.1. Experimental setup and boundary conditions

For the mechanical tests, a *ZwickRoell Z005* (ZwickRoell, Ulm, Germany) universal testing machine was utilized together with a 10 kN force cell. Additionally, a temperature furnace (ZwickRoell, Ulm, Germany) was incorporated in the experimental set-up for all test temperatures above room temperature. Monotonic, uniaxial tension tests were conducted in fiber direction (x-direction) and perpendicular to the fibers (y-direction) as displayed in Fig. 1 together with cyclic tests in both directions. In addition, monotonic uniaxial compression tests (z-direction) were performed to complete the set of in-plane material characteristics and determine differences in the material related to the loading direction. Here, cyclic tests were conducted as well. For all compression tests, a load string with a reversal cage was used that converts tensile forces to a compressive load to reduce the effort in changing the experimental set-up from tension to compression. In addition, a lubricant was used to reduce bulging of the specimens in line with DIN EN ISO 604.

To gain insight into the material behavior for multiaxial strain states, monotonic tension tests under varying fiber angle (15°, 30°, 45°, 60°) were conducted as well at room temperature and one elevated temperature (150°). For these tests, material from a second order was used that was made several month after the first one, thus a comparison between first and second batch of material will be given as well.

To obtain non-tactile displacement measurements, an *ARAMIS 4M* (Zeiss, Oberkochen, Germany) digital image correlation (DIC) system was exploited during testing. Therefore, the specimens were primed

with a white color coat, on which graphene speckles were applied in a secondary step to generate a stochastic pattern visible for the DIC system. Outside the temperature furnace, 3D DIC measurements were taken with two cameras for all tension tests, while testing at elevated temperatures required changing to a 2D set-up with one camera due to the small window of the temperature furnace and the reflections caused by the window pane. In these cases, major attention was paid to achieve a perpendicular alignment between the specimen surface and the camera lens with a translative motion test serving as a verification. The effect of barrel distortion or thinning of the specimen (change in distance to the camera) that could lead to differences between 2D and 3D measurements was tested in advance with several 2D room temperature tensile tests in the temperature furnace compared to the 3D results outside the temperature chamber see Fig. 6(a). In general, the 2D measurements resulted in a softer material behavior compared to the measurements with two cameras. The deviation in y-direction is negligible, in x-direction, however, a significant change in stiffness is present. The authors believe that this difference does not only result from the change between 2D and 3D DIC measurements but is influenced by several factors such as the window pane of the temperature chamber and the smaller specimen size. As a consequence of the blurring effect of the window pane and the increased distance between camera and specimen, it was necessary to adjust the stochastic pattern to a coarser grid. This resulted in a reduction in the number of interpretable data points, particularly in x-direction, where the number of available data points was significantly decreased due to the smaller specimen dimensions. Without the change in speckle size, however, the camera was unable to focus, and thus the adjusted stochastic pattern served to mitigate the issue caused by the temperature furnace. Though explainable, the measurement differences will be visible in the upcoming results in fiber direction and need to be interpreted with care. Here, a better camera system and more light sources, especially in the blue light range, could lead to an improvement. Additionally, indirect lighting from the side window of the temperature furnace could be considered. In terms of the compression tests, only 2D DIC measurements were possible at room temperature since the distance between the specimen and the camera needed to be reduced due to the small specimen size. For the compression tests above room temperature, unfortunately, no DIC measurements were possible. This can be attributed mostly to the reversal cage that caused severe shadowing on the backwards offset specimen in combination with the light sources arranged at an angle to the window pane to reduce reflection. The use of compression plates that were not available at that time would improve the set-up and reduce shadowing. Nonetheless, the increased distance between the camera and the specimen due to the temperature furnace would need to be resolved as well. In total, experiments were conducted at three distinct temperatures, both below and above the glass transition temperature of the matrix material ($T_g \approx 58$ °C, cf. Reuvers et al., 2024): 23 °C, 100 °C, and 150 °C. The heating time for achieving a homogeneous temperature distribution across the specimens measured 15 min prior to testing for the tensile specimens and 30 min for the compression specimens due to the increased thickness. To allow for thermal expansion, the tension specimens were clamped only at the upper part during heating.

To ensure comparability with the tests conducted in Reuvers et al. (2024), two strain rates ($\dot{\varepsilon}^t_{\text{min}} = 2.1$ mm/min and $\dot{\varepsilon}^t_{\text{max}} = 4.2$ mm/min) were prescribed for all tension tests independent of the fiber direction to study the rate dependent material behavior that is reported for PA6 (see e.g. Shan et al., 2007; Ayoub et al., 2011). Hereby, the loading rate was controlled by the cross head speed of the machine. In terms of the loading rate for the compression tests $\dot{\varepsilon}^c_{\text{min}} = 0.3$ mm/min and $\dot{\varepsilon}^c_{\text{max}} = 3.0$ mm/min were used. Converted to the dimensions of the respective specimens, the lowest loading rate for each test corresponds to 0.0005 s^{-1}, as used for the experiments on PA6 blends in Reuvers et al. (2024). The tests were terminated once the specimen broke or the maximum force of the testing machine (5 kN) was reached. Each procedure was repeated three to four times. The strain data was obtained using the DIC data averaged over the whole specimen domain, whereas the force data was taken directly from the *ZwickRoell* machine. To avoid effects due to imperfect stochastic pattern or imperfections during cutting, the area close to the specimen edge was excluded from the evaluation of the DIC measurements. All results are given in terms of engineering stress ($P = F/A_0$) ,defined as the current force F divided by the undeformed cross-sectional area A_0, over engineering strain ($\varepsilon = \Delta L/L$), defined as the ratio of the change in length ΔL to the original length of the specimen L.

Lastly, three-point bending tests were conducted at room temperature in x- and y-direction to determine the Young's modulus in bending as well as the flexural stress–strain response of the material. Here, DIC measurements were omitted, due to the short distance between load cell and cross head in this set-up which reduces the slip significantly.

2.4.2. Experimental results

Fig. 3 shows the results for the monotonic tension tests in and perpendicular to the fiber direction at room and elevated tests temperatures. Here, the experimental average is given together with the deviation in terms of maximum and minimum stress of the test series. In fiber direction ($x-$direction), the material response is linear at room temperature and only slightly nonlinear for elevated temperatures due to the high material stiffness and the machine limit of 5 kN. A clear temperature dependence is visible in y-direction, where a higher temperature generally leads to a reduction in material stiffness. The temperature dependence in $x-$direction most likely results from the difference in 2D between 3D DIC measurements, as discussed in Section 2.4.1. Furthermore, the strain rate dependence is more pronounced at higher temperatures. Unfortunately, the tests in $x-$direction for the lowest strain rate at 150 °C are not usable since the exposure to temperature during pre-heating, combined with the longer testing time, led to sliding of the specimens in the clamping area. After testing, shear marks were visible on the specimens in the clamping area (see Fig. 3), where the bracket was in contact with the fibers due to the increased viscosity of the PA6 matrix at 150 °C. Consequently, the low friction resistance of the glass fibers compared to the polymer matrix caused sliding. A reinforcement with CFK at the clamping area did not improve the test results. Consequently, they were left out of the plot. Here, pneumatic grips might improve the test situation. For the tests with higher velocity, the problem was less pronounced due to the reduced contact time. Note here that sliding occurred only in fiber direction. Compared to the tests in fiber direction, in transverse direction, the temperature dependence of the material response is more pronounced in line with Gröger et al. (2021) who tested the same material system. Here, the matrix material, which shows a pronounced temperature sensitivity (cf. Shan et al., 2007; Felder et al., 2020b and Reuvers et al., 2024) in the considered temperature range, dominates the material response. Moreover, a more gradual roll-over to yielding is observed for temperatures above the glass transition, where a highly nonlinear material response is visible. Overall, the strain rate dependence is more distinct in y-direction. Similarly to the results in x-direction, the sensitivity to the loading velocity increases with increasing temperature. Fiber sliding was observed in both directions, especially at room temperature, where the matrix material is less ductile. Here, the debonding or rupture of individual fibers led to kinks in the individual force displacement curves and, therefore, resulted in a higher deviation at elevated strains. In compression, the tests were conducted at two different strain rates with a decade difference. Therefore, here the dependence of the material response on the loading rate is more pronounced compared to the tensile tests.

In Fig. 4, the boundary conditions as well as the results for the stepwise cyclic tension tests are shown for an exemplary temperature of 150 °C. During the experimental procedure, the specimens were subjected to displacement controlled loading followed by an unloading step until the force equaled zero. A subsequent recovery step to

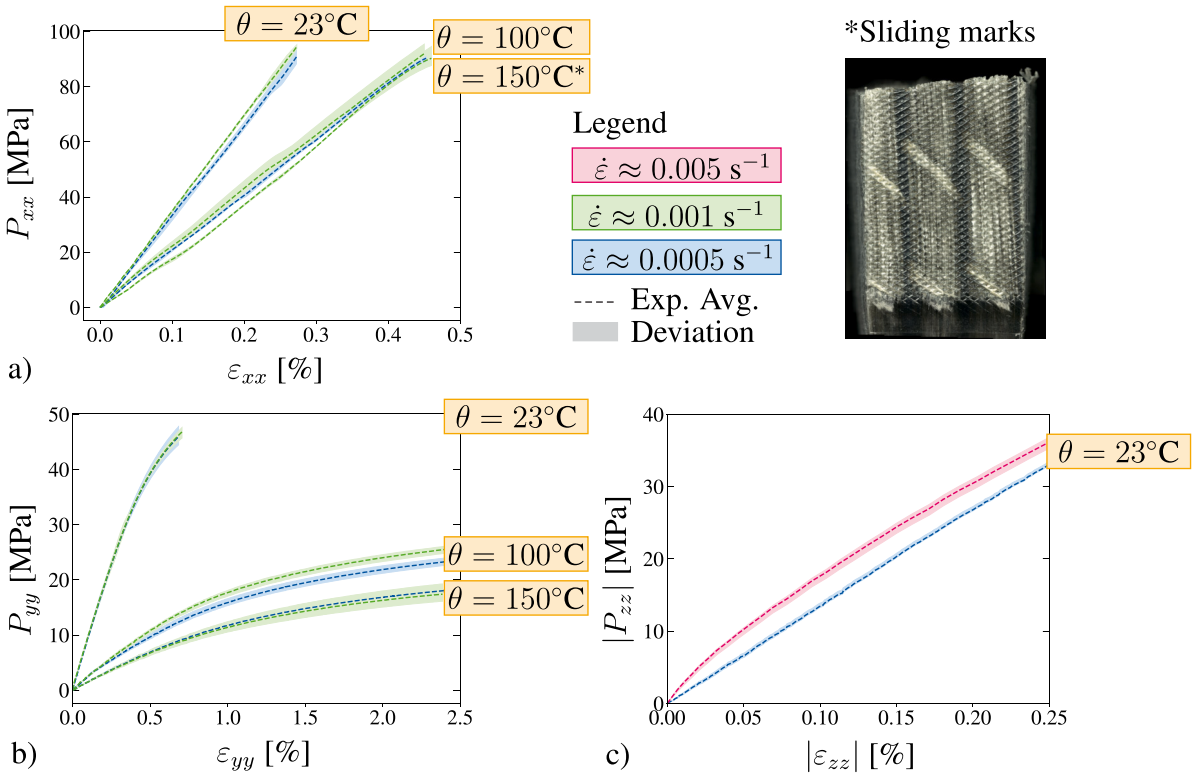

Fig. 3. (a) Monotonic, uniaxial extension in fiber direction. *Results only available for $\dot{\epsilon} \approx 0.001\ s^{-1}$ due to sliding at the clamp. (b) Monotonic, uniaxial extension results in transverse direction. (c) Monotonic, uniaxial compression in transverse direction for various strain rates.

distinguish between time-dependent and time-independent remaining deformations was omitted here due to the extensive relaxation times of the matrix material detected in Reuvers et al. (2024). The target displacements were determined based on the machine results from the monotonic tension tests to ensure comparability between the varying material directions. Moreover, high displacements were deliberately omitted to avoid slipping at the clamping areas, as observed in the monotonic tension tests (cf. Fig. 3). Due to the lower stiffness perpendicular to the fiber direction, an additional load step with $u_i/u_{\max,i} = 1\%$ was included to determine the elastic regime. The results of the cyclic tension tests at elevated temperature (see Fig. 4) show a distinct nonlinearity in the loading and unloading paths in both directions, however, more pronounced perpendicular to the fiber direction. In fiber direction, no remaining deformation is present for the first two load cycles. Thus, the authors conclude that plastic deformation occurs from the third load cycle onwards. The remaining deformation at the end of the loading–unloading procedure, however, measured only 0.1%. Perpendicular to the fiber direction, plastic deformations were already visible in the 5% load step, corresponding to the lower material stiffness in y-direction. Here, the final strain after testing measured approximately 1%. Interestingly enough, the hysteresis energy (area under the curve of each load step) seemed to increase with increasing deformation, especially for the results in y-direction. This observation suggests a deformation dependent visco-elastic material behavior as indicated by e.g. Reese and Govindjee (1998), Lion (1999), Holmes et al. (2006) and Amin et al. (2006) for the viscosity of polymeric materials and experimentally detected for PA6 by Felder et al. (2020b) and Reuvers et al. (2024).

In Fig. 5, the results for the experiments under varying fiber angle are shown. Firstly, the average material stiffness in GPa for each fiber angle is calculated from the monotonic tension tests according to DIN EN ISO 527-5 and plotted over the fiber angle. A severe and nonlinear reduction in material resistance is visible between the stiffness in fiber direction (°) and perpendicular to it (90°). Initially the material stiffness reduces drastically between fiber angles of 0° and 30°. Afterwards, the changes are only marginal, suggesting that between 45° and 90° the matrix material dominates the material response. Interestingly enough, the influence of the fibers on the overall material response appears to be temperature dependent. With increasing temperature, the fiber influence vanishes already at 30° which could be related to a weakened fiber–matrix-interface due to the increased matrix ductility. This trend, however, is only visible in the material stiffness and does not translate to the maximum force of the material shown in Fig. 5(b). Here, the fiber influence is still clearly visible at 30°. Note here that the test in fiber direction (0°) is left out since the machine maximum (≈ 5 kN) is already reached for a fiber angle of 15°. In both comparisons, the results for 90° lie slightly above the minima at 60° which can be attributed to testing on two material batches. During specimen production, the use of the diamond cutting blade, together with a water jet for cooling purposes, led to more offcuts. Consequently, a second order of material needed to be placed to substitute the loss. To ensure comparability, monotonic tension tests in x- and y–direction were repeated with the second batch and compared to the results for the first batch, see Fig. 6b. In fiber direction, no difference apart from the expected material scatter is visible. On the contrary, perpendicular to the fiber direction the response of the second batch appears to be slightly softer. The authors believe that the changes in the two batches stem purely from the polyamide 6 matrix and are therefore only prominently visible when testing perpendicular to the fibers, since the fibers themself dominate in this case. Though the orders were placed at different times, with significant temporal distance inbetween, the authors suspect that inconsistency in the individual components (PA6 granulate, roving glass sheets) is most likely not the reason for the differences. During production, the polyamide 6 matrix undergoes a phase transition from melt to solid and, additionally, crystallizes over a period of time. Here, the cooling rate mainly determines the resulting amount of crystalline phase. In contrast, the fibers do not change their material characteristics during the consolidation process. Moreover, the tested plates are not mass produced but rather a custom-built research

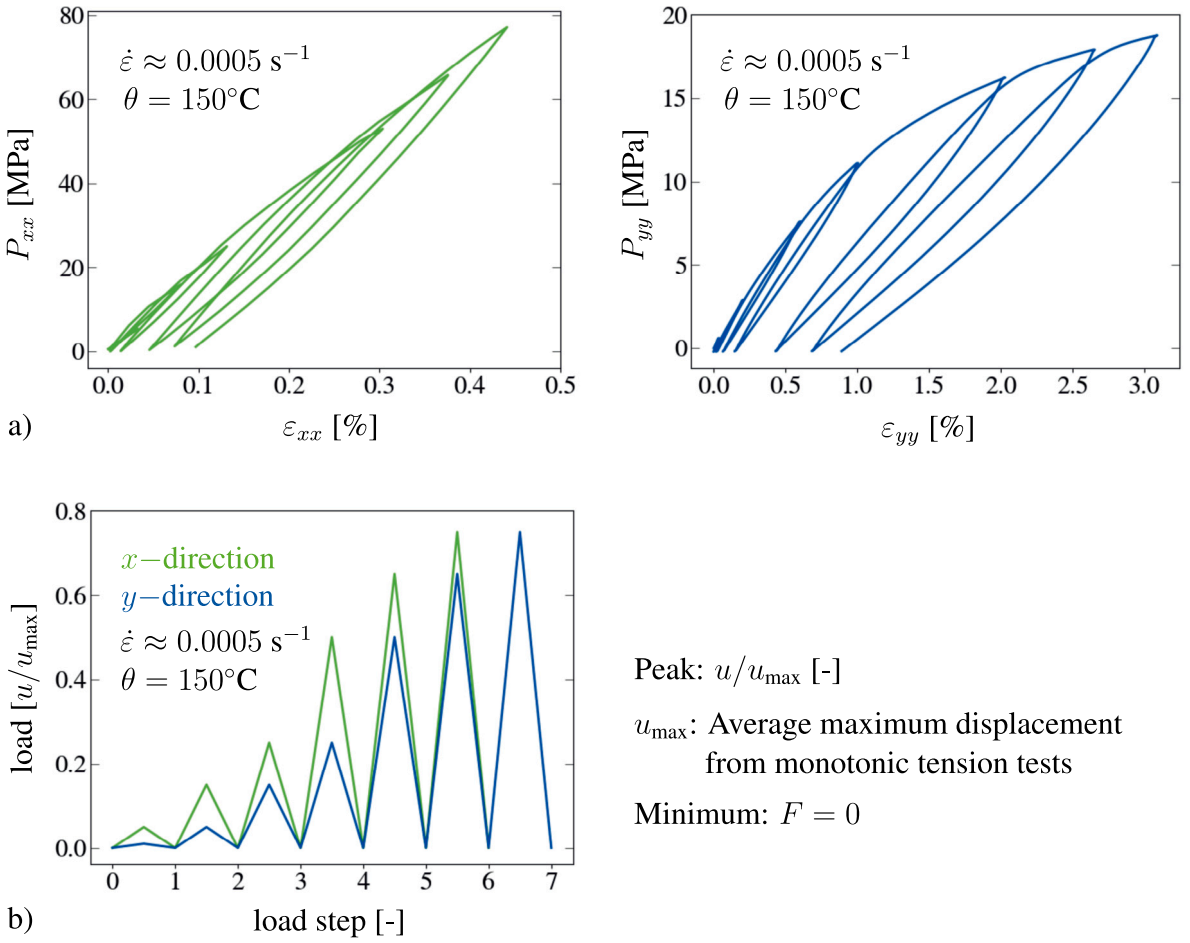

Fig. 4. (a) Cyclic tension results in fiber and transverse direction at 150 °C. (b) Boundary conditions for the cyclic tension tests.

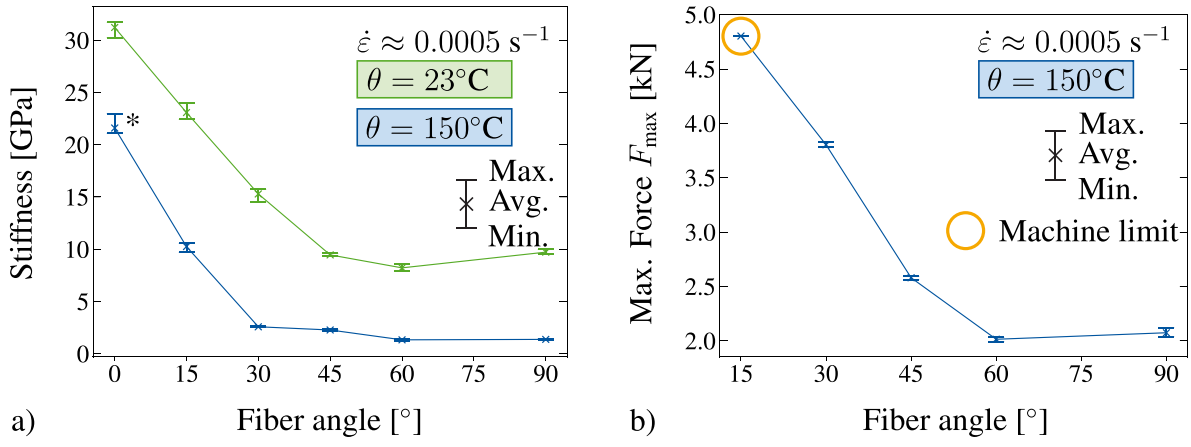

Fig. 5. Experiments under varying fiber angle (a) Material stiffness at various temperatures (* indicates sliding marks) (b) Maximum force.

material due to the non-standard material thickness. This high plate thickness could lead to unwanted temperature gradients during cooling down from the melt, and therefore to an inhomogeneous crystallization distribution. For this reason, the authors believe that the crystal configuration most likely differs between the plates and that the variance in the two batches (and most likely the majority of the material scatter as well) stems from the polyamide 6 matrix. Nonetheless, the differences between both material batches are negligibly small, and can only be seen in Fig. 5 where results from both batches are combined. In all other figures, either results from batch one or batch two are used.

The results of the three-point bending tests are shown in Table 2. Here, the test data at room temperature was enriched with results conducted at the Polymer Service Merseburg GmbH (PSM) at room and elevated test temperatures in line with DIN EN ISO 14125. The Young's modulus in bending E_f in x- and y-direction was measured together with the flexural strength σ_{fM} and the corresponding strain ϵ_{fM}.

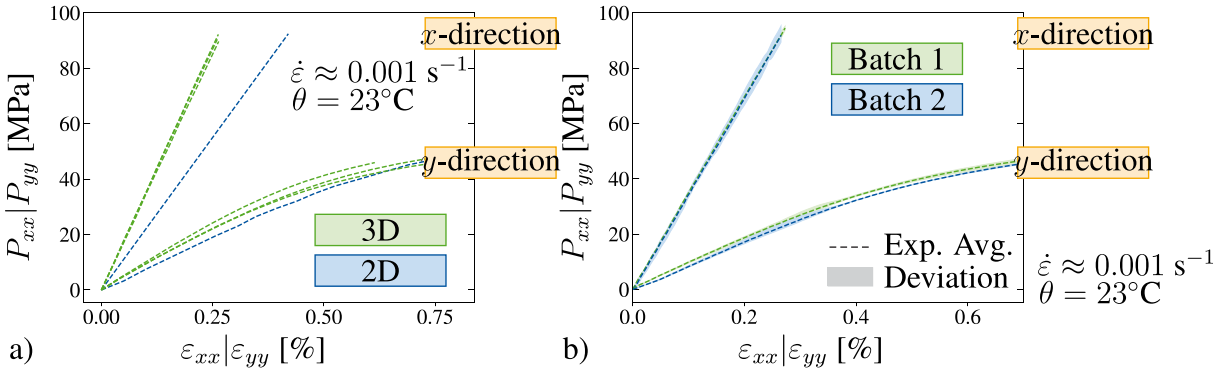

Fig. 6. Additional tests: (a) Comparison of 2D (inside the temperature furnace) and 3D (outside the temperature furnace) DIC measurements at room temperature. (b) Comparison of different material batches in x- and y-direction. (For interpretation of the references to color in this figure legend, the reader is referred to the web version of this article.)

Table 2
Three-point bending results in x- and y-direction at room and elevated temperatures.

	Temperature [°C]	Direction	E_f [MPa]	σ_{fM} [MPa]	ε_{fM} [%]	σ_{fB} [MPa]	ε_{fB} [%]
	23	x	30 531	850	2.78	850	2.78
s			650	28.3	0.11	28.8	0.092
	23	y	7327	96.3	1.97	96.3	1.97
s			303	3.22	0.146	3.22	0.146
	100	x	27 388	353	1.40	285	2.53
s			916	17.5	0.04	32.5	0.0923
	100	y	2445	57.2	4.07	52.8	4.24
s			82	1.34	0.17	2.52	0.21
	150	x	25 415	269	1.47	242	2.85
s			609	4.91	0.78	13.7	0.11
	150	y	1738	43.0	3.85	37.8	4.03
s			64	2.81	0.41	4.36	0.38

Where available, the breaking stress σ_{fB} and strain ε_{fB} are provided as well. Each test was repeated at least five times, hence all values are given as the statistical mean and the standard deviation s is shown as well below the results.

The results from Table 2 support the findings from the tensile tests in Figs. 3 and 5, where the material stiffness is temperature dependent and an increase in temperature generally leads to a decrease in material stiffness, especially perpendicular to the fibers. This relation holds for the maximum stress and the failure stress as well. However, here the temperature dependence is pronounced in x-direction as well. Moreover, at room temperature the failure behavior is brittle corresponding to $\sigma_{fM} = \sigma_{fB}$, whereas for elevated temperature a more ductile failure is observed. In x- direction, the material failed due to a combination of tension and compression, whereas in y-direction a tension failure was observed independent of the temperature.

2.5. Thermal analysis

The thermal analysis of the material was conducted at the Institute of Mechanics, University of the German Federal Armed Forces, Munich and Polymer Service GmbH Merseburg (PSM).

To obtain insights into the expansion of the material under temperature, a thermomechanical analysis was conducted on a TMA/SDTA841e from *Mettler Toledo* (Mettler Toledo, Columbus, USA) in all three material directions. In Fig. 7a, the resulting coefficients of thermal expansion (CTEs) α_T are plotted over the temperature. Here, the thermal expansion in fiber direction (x-direction) is least pronounced and reflects the lower thermal expansion of glass fibers according to the manufacturer (α = 4.9–5.1 10^{-6}/K) and in line with experiments from Segal (1979). Additionally, no distinct temperature influence is observed in this direction. On the other hand, the in-plane thermal expansion coefficients react sensitively to temperature, especially above the glass transition. However, interestingly enough, the thermal expansion in y- and z-direction does not coincide. Considering the microscopic images in Fig. 2, the authors believe that this observation is related to the production process (cf. Section 2.3), where the consolidation of prepregs results in a layer structure in z-direction. Consequently, in this direction, the polymeric matrix behavior is most pronounced, leading to an increased thermal expansion together with a strong temperature dependence above the glass transition, in line with the results for pure PA6 in Reuvers et al. (2024). In y-direction, the CTE lies in-between the results for the other two directions.

The thermal conductivity was measured on a *Hot-Disk* TPS 2500S (Hot Disk, Gothenburg, Sweden). For testing, the 1D *Hot-Disk* method was employed, utilizing a sensor with a diameter of 12.8 mm. This was deemed an appropriate choice given that larger sensors generally yield more accurate results. The method requires a cylindrical specimen with a diameter that is 2 mm greater than that of the sensor. Consequently, only the thickness direction (z-direction) was tested using the measured composite density of ρ = 1.8 g/cm^3 since the maximum thickness of the composite plate measured 10 mm in total. It is important to note that smaller sensors were available for testing, however, they did not produce reliable results for the polymeric material, which is generally low in conductivity. In Fig. 7b, the resulting thermal conductivity is plotted over the temperature. The composites' thermal conductivity is higher compared to that of pure PA6 which can be attributed to the influence of the glass fibers ($\lambda_{glassfiber} \approx 1.28$ W/m K). Similar to the results in Reuvers et al. (2024) for PA6, the influence of temperature on the resulting thermal conductivity is negligible, see also (Kugele, 2020). Therefore, from this point onwards, a transverse thermal conductivity of $\lambda_{T,\perp} = \lambda_{T,y} = \lambda_{T,z} = 0.6365$ W/m K is used in all calculations. Additionally, the authors expect to see no significant difference between the results in fiber and transverse direction in line with results from Kalaprasad et al. (2000) since the heat conductivity of the glass fibers is isotropic. To verify the assumption, virtual thermal experiments on the unit cell will be conducted in Section 5.2 in all material directions. Furthermore, the specific heat capacity is derived from the second heating run of the composite DSC experiments in Section 2.1. Here, the tangent to the experimental curve yields the specific heat capacity above and below the glass transition T_g, which increases with increasing temperature (see Fig. 7c)). Note here that the steep incline of the heat capacity after the melting of the crystalline phase is unexpected. Generally, the slope of c_T should be approximately equal below and above the glass transition. Thus, the authors suspect that structural changes might be the reason for this uncertainty.

3. Polymeric matrix material model formulation

The following section provides a brief overview of the material model utilized for the polyamide 6 matrix. For a more detailed description, the reader is kindly referred to Reuvers et al. (2024), where

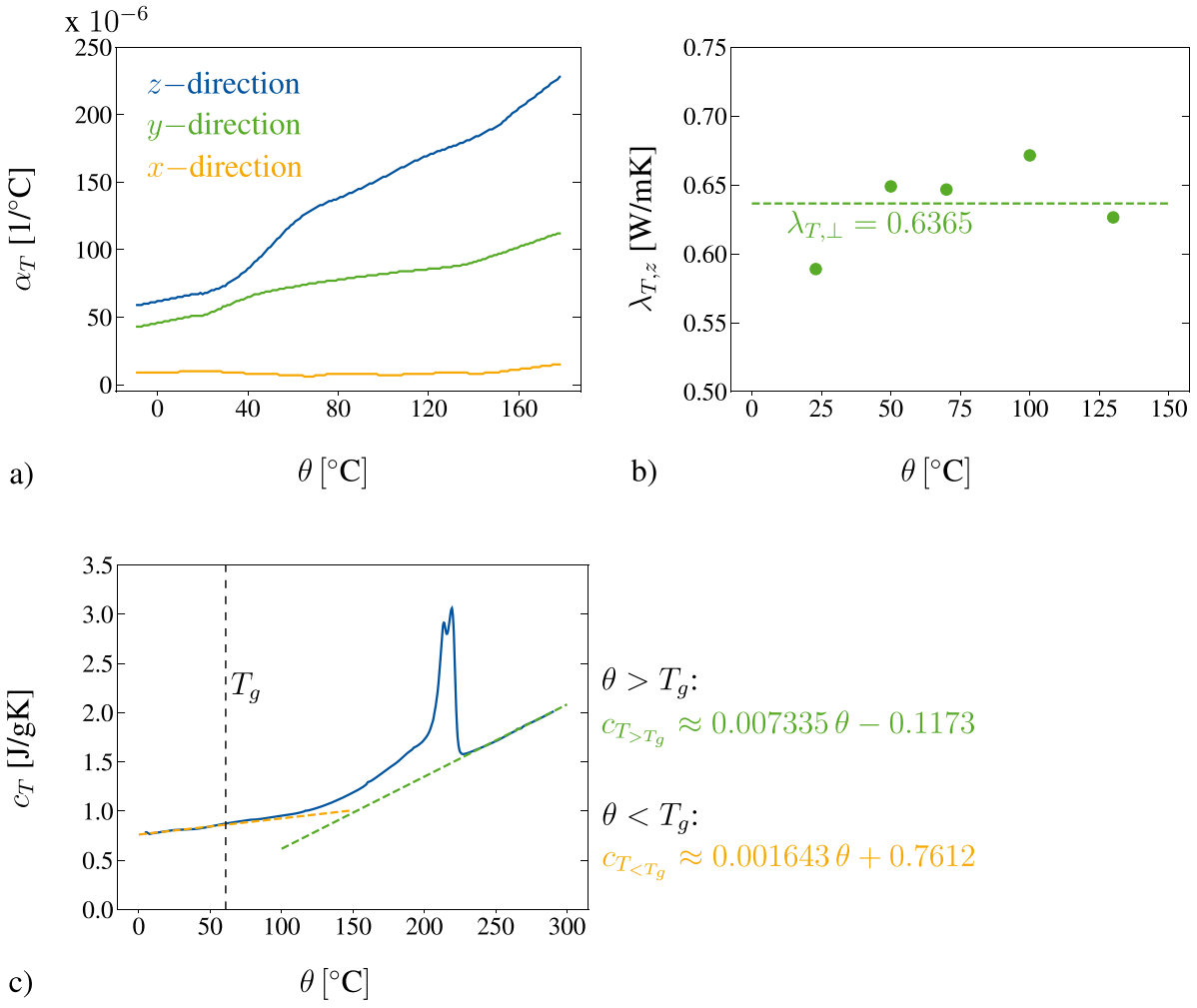

Fig. 7. Thermal analysis (a) Direction dependent coefficient of thermal expansion (TMA measurement) (b) Thermal conductivity measurement in z-direction (c) Specific heat capacity from DSC measurements in the second heating run.

the full derivation of the framework is presented together with the numerical implementation as a user material subroutine UMAT and UMATHT for the commercial finite element method (FEM) software Abaqus/Standard (Dassault Système, Vélizy-Villacoublay, France). Throughout the text, the subsequent notational conventions are employed:

a, A	Scalar quantity
$\boldsymbol{a}$	First order tensor
$\boldsymbol{A}$	Second order tensor
$\boldsymbol{I}$	Identity tensor
$\mathbb{A}$	Fourth order tensor
$\dot{(*)}$	Total derivative with respect to time
$(\boldsymbol{A})^T$	Transpose of $\boldsymbol{A}$
$(\boldsymbol{A})^{-1}$	Inverse of $\boldsymbol{A}$
$\mathrm{tr}(\boldsymbol{A})$	Trace of $\boldsymbol{A}$
$\det(\boldsymbol{A})$	Determinant of $\boldsymbol{A}$
$\mathrm{dev}(\boldsymbol{A})$	$\boldsymbol{A} - \frac{1}{3}\mathrm{tr}(\boldsymbol{A})\boldsymbol{I}$
$\mathrm{Grad}(\boldsymbol{A})$	Gradient of $\boldsymbol{A}$ with respect to the reference configuration
$\mathrm{Div}(\boldsymbol{A})$	Divergence of $\boldsymbol{A}$ with respect to the reference configuration
:	Double contraction
$\bar{(*)}$	Quantity in the reference configuration

To accurately capture the material behavior of semi-crystalline polymers (SCPs), a coupled visco-elastic, elasto-plastic framework is chosen, according to Reuvers et al. (2024). A schematic overview in the form of a 1D rheological representation of the model assumptions is provided in Fig. 8. Here, a multiplicative split of the deformation gradient $\boldsymbol{F}$

$$\boldsymbol{F} = \boldsymbol{F}_{e1}\,\boldsymbol{F}_p = \boldsymbol{F}_{e2}\,\boldsymbol{F}_v, \tag{2}$$

into elastic ($\boldsymbol{F}_{e1}$) and plastic ($\boldsymbol{F}_p$) (see e.g. Eckart, 1948; Kröner, 1959; Lee, 1969) as well as an elastic ($\boldsymbol{F}_{e2}$) and viscous ($\boldsymbol{F}_v$) part (see e.g. Sidoroff, 1974; Lubliner, 1985; Lion, 1997; Reese and Govindjee, 1998) is introduced. Further, an additional split of the plastic part of the deformation gradient $\boldsymbol{F}_p = \boldsymbol{F}_{pe}\,\boldsymbol{F}_{pi}$ (cf. Lion, 2000; Dettmer and Reese, 2004) is performed to model nonlinear kinematic hardening.

The Helmholtz free energy per unit mass is expressed in terms of symmetric elastic deformation measures only, namely the elastic right Cauchy–Green tensors $\boldsymbol{C}_{e1}$, $\boldsymbol{C}_{pe}$ and $\boldsymbol{C}_{e2}$ defined as

$$\boldsymbol{C}_{e1} = \boldsymbol{F}_{e1}^T\,\boldsymbol{F}_{e1}, \quad \boldsymbol{C}_{pe} = \boldsymbol{F}_{pe}^T\,\boldsymbol{F}_{pe}, \quad \boldsymbol{C}_{e2} = \boldsymbol{F}_{e2}^T\,\boldsymbol{F}_{e2}. \tag{3}$$

Here, $\boldsymbol{C} = \boldsymbol{F}^T\boldsymbol{F}$ denotes the right Cauchy–Green tensor and $\boldsymbol{C}_p = \boldsymbol{F}_p^T\boldsymbol{F}_p$ the plastic right Cauchy–Green tensor. Following the assumptions made in Fig. 8, the total specific Helmholtz free energy

$$\psi(\boldsymbol{C}_{e1}, \boldsymbol{C}_{e2}, \boldsymbol{C}_{pe}, \chi, \theta) = \psi_1(\boldsymbol{C}_{e1}, \boldsymbol{C}_{pe}, \chi, \theta) + \psi_2(\boldsymbol{C}_{e2}, \theta) + \psi_c(\theta) \tag{4}$$

is additively decomposed into elasto-plastic (ψ_1) and visco-elastic (ψ_2) energetic contributions accompanied by an unspecified caloric part ψ_c to ensure flexibility regarding the choice of the function for the heat capacity c_T (cf. Felder et al., 2022; Reuvers et al., 2024). Here, the first

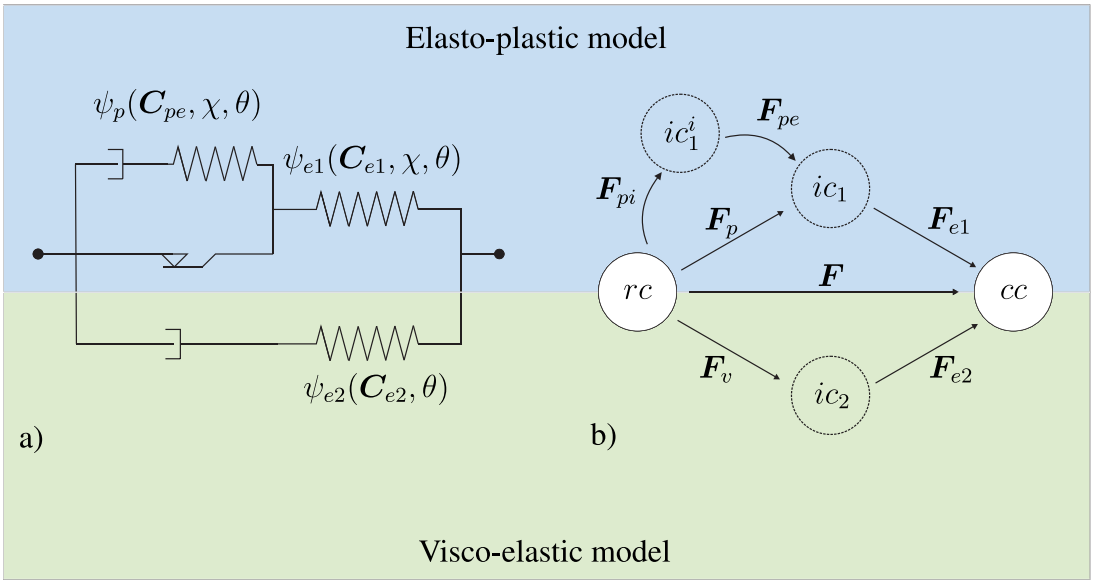

Fig. 8. (a) Schematic illustration of the constitutive model (b) Multiplicative splits of the deformation gradient (reference (rc) and current (cc) configurations, local intermediate configurations ic_1, ic_1^i and ic_2 for plasticity, kinematic hardening and viscosity).

term ψ_1 contains an elastic part ψ_{e1} as well as a defect energy ψ_p related to kinematic hardening

$$\psi_1(\boldsymbol{C}_{e1}, \boldsymbol{C}_{pe}, \chi, \theta) = \psi_{e1}(\boldsymbol{C}_{e1}, \chi, \theta) + \psi_p(\boldsymbol{C}_{pe}, \chi, \theta), \tag{5}$$

both dependent on the crystallization state of the material via the degree of crystallinity χ. The energy contributions related to the elasto-plastic model part ψ_1 are chosen as a compressible Neo-Hookean-type energy ψ_{e1} in combination with a nonlinear plastic defect energy ψ_p to account for Armstrong–Frederick kinematic hardening

$$\psi_{e1} = \frac{\mu_1}{2}\left(\mathrm{tr}(\boldsymbol{C}_{e1}) - 3\right) - \mu_1 \ln\left(J_{e1}\right) + \frac{\Lambda_1}{4}\left(\det(\boldsymbol{C}_{e1}) - 1 - 2\ln(J_{e1})\right) - 3\,K_1 \alpha_T\,\Delta\theta \ln(J_{e1}), \tag{6}$$

$$\psi_p = \frac{c}{2}\left(\mathrm{tr}(\boldsymbol{C}_{pe}) - 3\right) - c\ln(\sqrt{J_{pe}}). \tag{7}$$

Here, $J_{e1} = \det(\boldsymbol{F}_{e1})$ is the determinant of the elastic part of the deformation gradient $\boldsymbol{F}_{e1}$ and $J_{pe} = \det(\boldsymbol{C}_{pe})$ holds. In terms of the material quantities, the two Lamé constants $\mu_1(\chi, \theta)$ and $\Lambda_1(\chi, \theta)$ are introduced in ψ_{e1} and $c(\chi, \theta)$ in the defect energy ψ_p. The expression for the elastic energy ψ_{e1} in Eq. (6) is extended with a term related to volumetric thermal expansion incorporating the elasto-plastic bulk modulus[2] $K_1(\theta)$, the coefficient of thermal expansion $\alpha_T(\theta)$ and the temperature difference $\Delta\theta = \theta - \theta_0$ between the current temperature θ and the reference temperature θ_0. All material properties of the elasto-plastic part depend on both the DOC and temperature. Similarly to Eq. (6), the visco-elastic part of the Helmholtz free energy ψ_{e2} is defined as

$$\psi_2 = \frac{\mu_2}{2}\left(\mathrm{tr}(\boldsymbol{C}_{e2}) - 3\right) - \mu_2 \ln(J_{e2}) + \frac{\Lambda_2}{4}\left(\det(\boldsymbol{C}_{e2}) - 1 - 2\ln(J_{e2})\right) - 3\,K_2 \alpha_T(\theta - \theta_0)\ln(J_{e2}), \tag{8}$$

where $\mu_2(\theta)$ and $\Lambda_2(\theta)$ are the visco-elastic Lamé constants and K_2 is the visco-elastic bulk modulus[2]. Furthermore, $J_{e2} = \det(\boldsymbol{F}_2)$ holds. As indicated in Eq. (4), all energetic contributions jointly depend on the temperature θ.

[2] The bulk moduli $K_*, * = 1, 2$ are defined by the two Lamé constants μ_* and Λ_* as $K_* = \Lambda_* + \frac{2\mu_*}{3}$.

Next, the constitutive equations are derived from the local form of the Clausius–Duhem inequality

$$\boldsymbol{S} : \frac{1}{2}\dot{\boldsymbol{C}} - \rho_0(\dot{\psi} + \eta\,\dot{\theta}) - \frac{1}{\theta}\,\boldsymbol{q}_0 \cdot \mathrm{Grad}(\theta) \geq 0. \tag{9}$$

Here, $\boldsymbol{S}$ is the second Piola–Kirchhoff stress tensor and ρ_0 represents the material density per unit reference volume. The entropy is introduced via the parameter η and the heat flux in the reference configuration is denoted by $\boldsymbol{q}_0$ with the temperature dependent heat conductivity $\lambda_T(\theta)$. Following several mathematical operations (cf. Reuvers et al., 2024) the stress quantities are introduced as:

Second Piola–Kirchhoff stresses:

$$\boldsymbol{S}_1 = 2\rho_0 \boldsymbol{F}_p^{-1} \frac{\partial \psi_{e1}}{\partial \boldsymbol{C}_{e1}} \boldsymbol{F}_p^{-T}, \qquad \boldsymbol{S}_2 = 2\rho_0 \boldsymbol{F}_v^{-1} \frac{\partial \psi_2}{\partial \boldsymbol{C}_{e2}} \boldsymbol{F}_v^{-T}$$

Mandel stresses:

$$\boldsymbol{M}_1 = 2\rho_0 \boldsymbol{C}_{e1} \frac{\partial \psi_{e1}}{\partial \boldsymbol{C}_{e1}}, \qquad \boldsymbol{M}_2 = 2\rho_0 \boldsymbol{C}_{e2} \frac{\partial \psi_2}{\partial \boldsymbol{C}_{e2}}.$$

Back stress:

$$\boldsymbol{X} = 2\rho_0\, \boldsymbol{F}_{pe} \frac{\partial \psi_p}{\partial \boldsymbol{C}_{pe}} \boldsymbol{F}_{pe}^T$$

Mandel stress related to kinematic hardening:

$$\boldsymbol{M}_{1,\mathrm{kin}} = 2\rho_0\, \boldsymbol{C}_{pe} \frac{\partial \psi_p}{\partial \boldsymbol{C}_{pe}}$$

In terms of the evolution equations (see Table 3) a Tschoegl-type or paraboloid yield criterion (see e.g. Tschoegl, 1971; Ghorbel, 2008; Melro et al., 2013b) is adopted for the elasto-plastic part introducing the initial yield stress in compression σ_c^0 and tension σ_t^0. For the evolution of plasticity an associative flow rule is chosen together with the classical evolution equation for nonlinear Armstrong–Frederick kinematic hardening (Armstrong et al., 1966). Here, the plastic multiplier $\dot{\lambda}_p$ is introduced, as well as the hardening material parameters b and c. The evolution equation for the visco-elastic part is based on a potential from Reese and Govindjee (1998). For the specific choice of the nonlinear function for the relaxation time τ, the reader is kindly referred to Section 5. In addition, the local form of the energy balance

$$\rho_0\,(\dot{\psi} + \dot{\eta}\,\theta + \eta\,\dot{\theta}) + \mathrm{Div}(\boldsymbol{q}_0) - \boldsymbol{S} : \frac{1}{2}\dot{\boldsymbol{C}} = 0 \tag{10}$$

Table 3
Overview over the constitutive equations in the reference configuration.

Elasto-plastic contribution	Visco-elastic contribution
Stresses $\boldsymbol{S}_1 = \mu_1(\boldsymbol{C}_p^{-1} - \boldsymbol{C}^{-1}) + \frac{\Lambda_1}{2}\left(\frac{\det(\boldsymbol{C})}{\det(\boldsymbol{C}_p)} - 1\right)\boldsymbol{C}^{-1} - 3K_1\alpha_T(\theta - \theta_0)\boldsymbol{C}^{-1}$ $\bar{\boldsymbol{X}} = c\,(\boldsymbol{C}_{pi}^{-1} - \boldsymbol{C}_p^{-1})$ $\boldsymbol{Y} = \boldsymbol{C}\boldsymbol{S}_1 - \boldsymbol{C}_p\bar{\boldsymbol{X}}, \quad \boldsymbol{Y}_{\text{kin}} = \boldsymbol{C}_p\bar{\boldsymbol{X}}$ Yield function $\boldsymbol{\Phi}_p = 3\,J_2 + (m-1)\,\sigma_t^0\,I_1 - m\,(\sigma_t^0)^2$ $I_1 = \text{tr}(\boldsymbol{Y}), \quad J_2 = \frac{1}{2}\,\text{tr}((\text{dev}(\boldsymbol{Y}))^2), \quad m = \sigma_c^0(\chi,\theta)/\sigma_t^0(\chi,\theta)$ Evolution equations $\dot{\boldsymbol{C}}_p = \dot{\lambda}_p\,(6\,\text{dev}(\boldsymbol{Y}) + 2\,(m-1)\,\sigma_t^0)\,\boldsymbol{C}_p, \quad \dot{\boldsymbol{C}}_{pi} = 2\,\dot{\lambda}_p\,\frac{b}{c}\,\text{dev}(\boldsymbol{Y}_{\text{kin}})\,\boldsymbol{C}_{pi}$ $\dot{\lambda}_p \geq 0, \quad \boldsymbol{\Phi}_p \leq 0, \quad \dot{\lambda}_p\,\boldsymbol{\Phi}_p = 0$ Heat generation due to plastic dissipation $r_1 = \bar{r}_p = \frac{1}{2}\,\boldsymbol{C}\left(\boldsymbol{S}_1 - \theta\,\frac{\partial \boldsymbol{S}_1}{\partial\theta}\right) : \boldsymbol{C}_p^{-1}\,\dot{\boldsymbol{C}}_p - \frac{1}{2}\left(\bar{\boldsymbol{X}} - \theta\,\frac{\partial\bar{\boldsymbol{X}}}{\partial\theta}\right) : \dot{\boldsymbol{C}}_p$ $+\frac{1}{2}\,\boldsymbol{C}_p\left(\bar{\boldsymbol{X}} - \theta\,\frac{\partial\bar{\boldsymbol{X}}}{\partial\theta}\right) : \boldsymbol{C}_{pi}^{-1}\,\dot{\boldsymbol{C}}_{pi}$	Stress $\boldsymbol{S}_2 = \mu_2(\boldsymbol{C}_v^{-1} - \boldsymbol{C}^{-1}) + \frac{\Lambda_2}{2}\left(\frac{\det(\boldsymbol{C})}{\det(\boldsymbol{C}_v)} - 1\right)\boldsymbol{C}^{-1}$ $-3\,K_2\,\alpha_T\,(\theta - \theta_0)\boldsymbol{C}^{-1}$ Evolution equation $\dot{\boldsymbol{C}}_v = \left(\frac{1}{\tau\mu_2}\,\text{dev}(\boldsymbol{C}\boldsymbol{S}_2) + \frac{2}{9\tau K_2}\,\text{tr}(\boldsymbol{C}\boldsymbol{S}_2)\,\boldsymbol{I}\right)\boldsymbol{C}_v$ Heat generation due to viscous dissipation $r_2 = \bar{r}_v = \frac{1}{2}\,\boldsymbol{C}\left(\boldsymbol{S}_2 - \theta\,\frac{\partial \boldsymbol{S}_2}{\partial\theta}\right) : \boldsymbol{C}_v^{-1}\,\dot{\boldsymbol{C}}_v$
Second Piola–Kirchhoff stress $\boldsymbol{S} = \boldsymbol{S}_1 + \boldsymbol{S}_2$	Elastic heat generation $r_e = \theta\left(\frac{\partial \boldsymbol{S}_1}{\partial\theta} : \frac{1}{2}\,\dot{\boldsymbol{C}} + \frac{\partial \boldsymbol{S}_2}{\partial\theta} : \frac{1}{2}\,\dot{\boldsymbol{C}}\right)$
Heat flux $\boldsymbol{q}_0 = -J\,\lambda_T\,\boldsymbol{C}^{-1}\,\text{Grad}(\theta)$	Entropy $\eta = -\partial\psi/\partial\theta$

is evaluated, to determine the internal heat sources. Above, the time derivative of the internal energy $\dot{e} = \dot{\psi} + \dot{\eta}\,\theta + \eta\,\dot{\theta}$ is already incorporated. In line with e.g. Felder et al. (2020a, 2022) and Reuvers et al. (2024), the heat capacity is approximated by a constant value $c_T = -\theta\,(\partial^2\psi)/(\partial\theta^2) = c_T(\chi,\theta)$ in this work and determined experimentally. The specific expression for c_T above and below the glass transition regime can be found in Table 9. An overview of the equations in their final form in the reference configuration is provided in Table 3.

4. Generation of repeating unit cells and comparison of different randomization methods

In this section, the generation of repeating unit cells (RUCs) is described in detail. Various randomization methods for the distribution of unidirectional glass fibers are tested and compared to microscopic pictures of the PA6 composite material used for the experiments in Section 2. Furthermore, mesh and size convergence studies are conducted to identify a valid RUC that will be used for comparison with the experimental results. Throughout the generation of the RUCs, the focus lied on the process automation to minimize the effort for e.g. the convergence studies. Therefore, the Abaqus - Python interface was used to generate a plug-in application that allows for automatic RUC generation and testing with mechanical and thermal periodic boundary conditions (PBCs).

4.1. Unit cell generation

The automatic generation of repeating unit cells is separated into three main steps. Firstly, the random distribution of the UD fibers is carried out using three different randomization methods. Next, the geometry of the unit cell is generated, followed by the automatic generation of the mesh and the corresponding periodic boundary conditions (PBCs). The input parameters for the Abaqus-Python plug-in are the constant fiber volume fraction $\varphi_f = 40\%$ and the diameter of the roving glass fibers (17 μm) as well as the number of fibers n_f that determine the size of the RUC. The fibers are modeled as cylinders under the assumption of a perfectly round cross-section, and no inhomogeneities along the fiber direction. Note here that the fibers in weft direction needed for structural support during production (approximately 3% of the total fiber volume content) are neglected. Moreover, the height and width of the RUCs are chosen to be equal, in that way, the dimensions of the RUC are a priori known when evaluating the input quantities given above. Three different randomization schemes are used to generate the random fiber distribution, namely the so-called randomized method (see e.g. Poggenpohl et al., 2022b), the random sequential adsorption (RSA) method (see e.g. Hinrichsen et al., 1986) and a variation of the RSA method based on microscopic images, which is referred to as clustered RSA (CRSA) in the following.

The randomized method is based on a repetition of a regular grid of initially two fibers that resemble square closest packing in 2D (see Fig. 9a)). Each fiber is shifted by a random value with respect to its original position. Hereby, the shift is restricted such that overlapping of the individual fibers is prevented (see Fig. 9a)). The number of fibers for this randomization method is limited to certain even numbers ($n_{f,\text{randomized}} = 2n^2, n \in \mathbb{N}$), based on the base cell for square closest packing and the restriction to quadratic RUC dimensions.

RUCs resulting from the random sequential adsorption method consist of sequentially generated random fiber coordinates within the limits of the RUC size. Each fiber is placed in the RUC and only those fibers are adsorbed that do not overlap with already existing ones (see Fig. 10 a)). Otherwise, the coordinates are discarded, and new ones are generated until the desired fiber volume fraction is reached (see Fig. 9b)). In addition, narrow gaps between the fibers and small or rather sharp matrix regions in the corners or the edges (see Fig. 10b)) that lead to insufficient mesh quality or problems during mesh creation are prevented as well. This step is especially important since the mesh is generated automatically with a predefined element size. Therefore, mesh refinement in those areas is a priori not possible and would require manual intervention. In comparison, the RSA method shows a higher degree of clustering, whereas the fiber distribution in the RUCs generated with the randomized method is more even. These differences are reflected in the resulting RUC behavior and, therefore, as well in the resulting effective material properties of the composite, as will be shown in Section 4.3. Generally, both methods are suited to

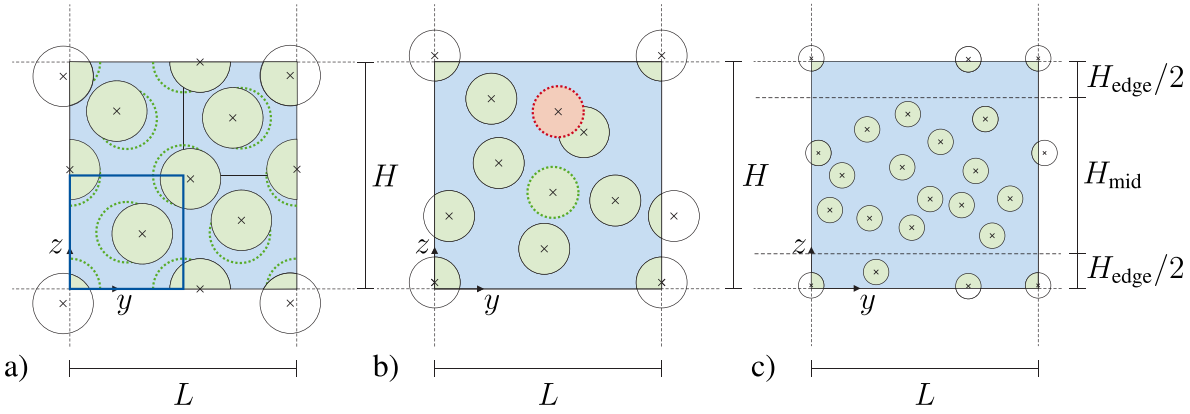

Fig. 9. Random fiber distribution generated with (a) randomized method (blue box marks base cell of two fibers) (b) random sequential adsorption (RSA) method (c) clustered RSA (CRSA) method. (For interpretation of the references to color in this figure legend, the reader is referred to the web version of this article.)

describe a random fiber distribution and the choice should be made on the basis of microscopic pictures. If, for instance, the fiber content is relatively high, however, the randomized method is the preferred choice since a valid fiber distribution with the RSA method is unlikely or requires various attempts that result in increased computation time. A saturation in the RSA approach with circular disks is reached with a maximum fiber volume fraction of approximately 54.7% according to the literature (cf. Feder, 1980; Hinrichsen et al., 1986). Comparing the microscopic images in Fig. 2 with images of RUCs with both randomization methods, the authors conclude that the RSA method better approximates the visible clustering of fibers. Nonetheless, areas can be indicated where no fibers are prominent, similar to a laminate structure. This effect stems from the production process, as discussed in Section 2.3. However, the laminate like structure is not incorporated in the RUCs yet. Thus, a third set of RUCs is generated for comparison using a variation of the RSA method, here referenced as clustered RSA (CRSA). To achieve a higher degree of fiber clustering, the assumption is made that the majority of the fibers lie in the middle of the RUC, while the upper and lower edge consists mainly of matrix material, see Fig. 9(c) for a visual reference. To achieve a random fiber distribution in each part, the RSA method is used. The resulting new parameters, namely the height of the middle area $H_{\text{mid}} = H - H_{\text{edge}}$ and the fiber volume content in this part $\varphi_{\text{mid}} = \varphi_{\text{fibers}} - \varphi_{\text{edge}}$ of the RUC need to be determined. Here, values between 0.5 and 0.9 for the ratio of H_{mid}/H and values between 0.75 and 0.95 for the ratio of the fiber volume fraction $\varphi_{\text{mid}}/\varphi_{\text{fibers}}$ are realized in a preliminary parametric study and further tested and visually compared to the microscopic pictures. In addition, it is made sure that the resulting RUC behavior differed from that of the RUCs generated with the RSA method, resulting in $H_{\text{mid}}/H = 0.6$ and $\varphi_{\text{mid}}/\varphi_{\text{fibers}} = 0.9$. It should be noted that the clustered RSA method results in varying material behavior in y- and z-direction (see Section 4.3), thus thwarting the assumption of transversal isotropy. Consequently, experiments in all three directions are necessary to validate this method.

After the fiber distributions are found and the geometries are generated using a sequence of boolean cuts, the mesh is generated automatically using eight node hexahedral elements with reduced integration (C3D8RT) from the Abaqus element library. Their performance has been compared to fully integrated elements for several uniaxial strain states combined with the RSA method. Here, the computation time of the reduced elements was significantly lower compared to the fully integrated elements, especially, due to the large history array of the complex nonlinear matrix material model. In the next step, periodic boundary conditions are created from the node set, applying Abaqus specific so-called equation constraints at the edges, faces and vertices of the RUC that mirror the local fluctuations of the current configuration at the respective boundaries. More specifically, PBCs prescribe a constant difference in displacement and/or temperature between nodes that share the same reference coordinates in all but one direction (see e.g. Miehe, 2002; Kanit et al., 2003; Nguyen et al., 2011). Hereby, the difference in displacement and/or temperature can either be zero or non-zero depending on the applied far field strain or temperature state. During the generation of the PBCs it is made sure that no node is over-constraint by excluding the respective nodes from the node sets of the edges, faces and vertices. For a detailed description on how to apply Abaqus specific displacement equation constraints, the reader is kindly referred to Omairey et al. (2019). An example for temperature equation constraints can be found in Tian et al. (2019).

The material model formulation used for the polyamide 6 matrix material can be found in Section 3 with the experimentally identified mechanical parameters in Appendix A.1. For the fibers, an isotropic linear thermo-elastic material model from the Abaqus material library was chosen for simplicity, since the glass fibers behave purely elastically over the considered temperature range ($\theta = 23 - 150°C$). The corresponding material parameters can be found in Section 5.

4.2. Homogenization scheme

Based on the hypothesis of equal virtual work density on the microscopic ($*_m$) and macroscopic ($*_M$) level, the Hill–Mandel condition (see Hill, 1963, 1967) with the thermal extension by Özdemir et al. (2007) states the equivalence of the product of the volume averages and the volume average of the products for a representative volume on the micro level

$$\delta W_M = \{\delta W_m\}_{\Omega_0} \tag{11}$$

$$\Leftrightarrow$$

$$\begin{aligned}&\{\boldsymbol{P}_m\}_{\Omega_0} : \{\delta \boldsymbol{F}_m\}_{\Omega_0} - \{\boldsymbol{q}_{0,m}\}_{\Omega_0} \cdot \{\text{Grad}_m(\theta_m)\}_{\Omega_0} \\ &= \{\boldsymbol{P}_m : \delta \boldsymbol{F}_m\}_{\Omega_0} \quad - \{\boldsymbol{q}_{0,m} \cdot \text{Grad}_m(\theta_m)\}_{\Omega_0},\end{aligned} \tag{12}$$

with the microscopic first Piola–Kirchhoff stress tensor $\boldsymbol{P}_m$ and the conjugated deformation gradient $\boldsymbol{F}_m$ as well as the microscopic heat flux $\boldsymbol{q}_{0,m}$ with respect to the reference configuration and the temperature gradient $\text{Grad}_m(\theta_m)$. In line with (Özdemir et al., 2007), the time variation of the heat storage on the microscale is neglected due to the negligibly small representative volume. Here, $\{*\}_{\Omega_0}$ denotes the volume average

$$\{*\}_{\Omega_0} = \frac{1}{V_{\Omega_0}} \int_{\Omega_0} (*) \text{dV}, \tag{13}$$

with V_{Ω_0} as the volume of Ω_0. The displacement as well as the temperature PBCs described in Section 4.1 are known to satisfy the Hill–Mandel

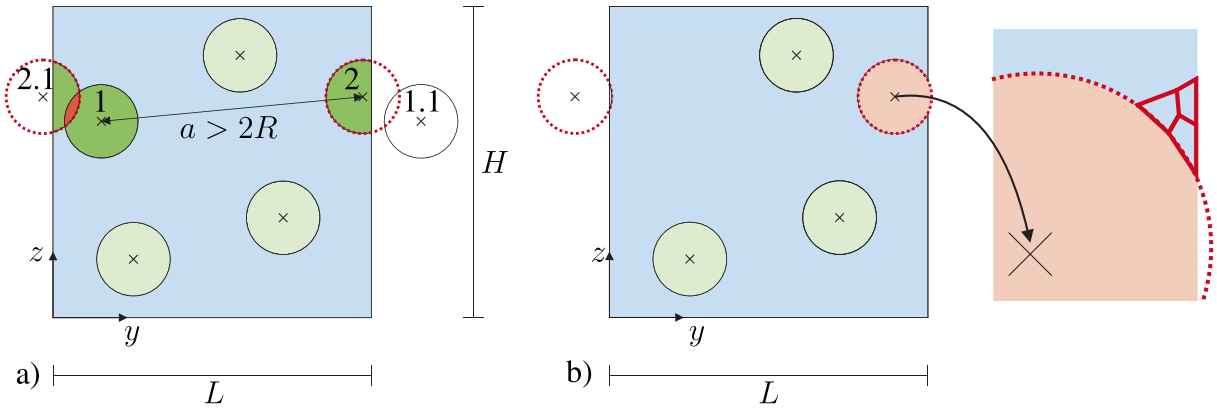

Fig. 10. (a) Rejection of overlapping fibers after projection (b) Abortion of fiber coordinates that lead to narrow gaps and sharp corners to circumvent poor mesh quality.

condition (cf. Van der Sluis et al., 2000; Özdemir et al., 2007). Consequently, the stress of a macroscale material point $\boldsymbol{P}_M$ complies with the averaged stress of a volume element on the microscale and the same relation holds for the heat flux

$$\boldsymbol{P}_M = \{\boldsymbol{P}_m\}_{\Omega_0} \tag{14}$$

$$\boldsymbol{q}_{0,M} = \{\boldsymbol{q}_{0,m}\}_{\Omega_0}. \tag{15}$$

Using Abaqus specific equation constraints, $\boldsymbol{P}_M$ is obtained from the reaction force of the corresponding reference point divided by the reference area (see e.g. Omairey et al., 2019). To obtain the elastic effective material parameters in the three material directions, six uniaxial strain states are applied successively on the RUCs under isothermal conditions at each test temperature. The corresponding tensile or shear loading conditions are shown schematically in Fig. 11 together with the associated material parameters. The macroscopic heat flux $\boldsymbol{q}_{0,M}$ equally follows from the averaged heat flux over the RUC domain, assuming stationary heat conduction. In order to obtain the direction dependent effective thermal conductivity a temperature gradient is applied successively on two opposing sides in each material direction (cf. Tian et al., 2019). Since the effect of the temperature on the conductivity of the GFRP is negligibly small (cf. Section 2.5), the effective thermal conductivity is calculated in Section 5 independently of the temperature.

4.3. Statistical evaluation

In this section, the representativeness of the RUCs is examined in a statistical manner. Therefore, several convergence studies are conducted to investigate the fluctuations introduced by the random fiber distributions. Note here that the investigations are carried out up to 5% maximum strain in line with the experimental results of Section 2. To model larger deformations, these convergence studies need to be extended to verify the RUCs. This is, however, omitted here to reduce the computational effort.

Mesh convergence study

For the mesh convergence study, three RUC geometries generated with the randomization methods from Section 4.1 are considered. The corresponding in-plane dimensions are derived from the number of fibers and the fiber volume fraction ($\varphi = 40\%$) and measure 116.7 μm × 116.7 μm for the RSA and CRSA method with $n_f = 24$ and 101.07 μm × 101.07 μm for the randomized method with $n_f = 18$. In fiber direction, only one element over the thickness is considered, which results in a material behavior comparable to plane strain. Different mesh sizes ranging from 1 to 3 μm are evaluated in steps of 0.5 μm. Regarding the boundary conditions, a constant temperature of 150 °C is chosen since at elevated temperatures, plastic yielding in the PA6 matrix occurs already at small strains compared to room temperature (cf. Table 8). Here, the highest DOC of the matrix $\chi = 0.29$ is used to determine the matrix material parameters from Table 8. Monotonic, uniaxial tension in y-direction is the tested load case (see Fig. 11 a2). The simulations are terminated at a strain of 5% and the resulting stresses and strains are computed as volume averages of the whole domain Ω_0. In Fig. 12a), the homogenized stresses at maximum strain are shown over the element size for the different randomization methods.

For the RSA and the CRSA method, a pronounced mesh dependence is visible, whereas the results of the randomized method show almost instantaneously converged behavior. This can be attributed to the lower amount of fiber clustering in the randomized method. Comparing the RSA based methods in more detail, a direct correlation between the amount of fiber clustering and the mesh convergence is visible. The higher the amount of fiber clustering, the smaller element size is needed to achieve a converged result. Next, to determine the mesh size at which convergence is achieved, the relative errors are computed as the difference in the resulting homogenized stress from the current mesh size compared to the stress of the next coarser mesh. Here, a change <1% is regarded as a converged solution. Overall, mesh convergence is achieved for all three fiber distributions. In terms of the randomized method, an element size of 2.5 μm is already assumed to show the converged solution, whereas for the RSA and CRSA method a size of 1.0 μm is sufficient. Therefore, a mesh size of 1.0 μm is adopted for the subsequent simulations.

Size convergence study

A size convergence study is performed for varying sizes of RUCs generated with all three randomization methods. Again, the number of fibers n_f is used as a measure for the overall RUC size since the fiber volume fraction and the fiber diameter are assumed to be constant. Due to the random fiber distribution, for every randomization method and number of fibers, 10 different RUCs are generated. Hence, the average is used for comparison together with the standard deviation indicated by the error bars. The RUCs are tested in in-plane tension (y-direction) and in-plane shear (yz-direction) (see Fig. 11 a2 and b3). Further, in-plane tension simulations in z-direction are conducted for the CRUCs to investigate their direction dependence. Similar to the convergence study for the mesh density, the stresses and strains are computed as volume averages of the whole domain Ω_0 and the computation is terminated at a maximum strain of 5%.

The results of the size convergence study are shown in Fig. 12b) and c) for both loading cases. In line with the results for the mesh density study, the randomized method yields almost instantaneously converged results for all RUC sizes. Moreover, compared to the other two methods, the standard deviation is very small, due to the low amount of fiber

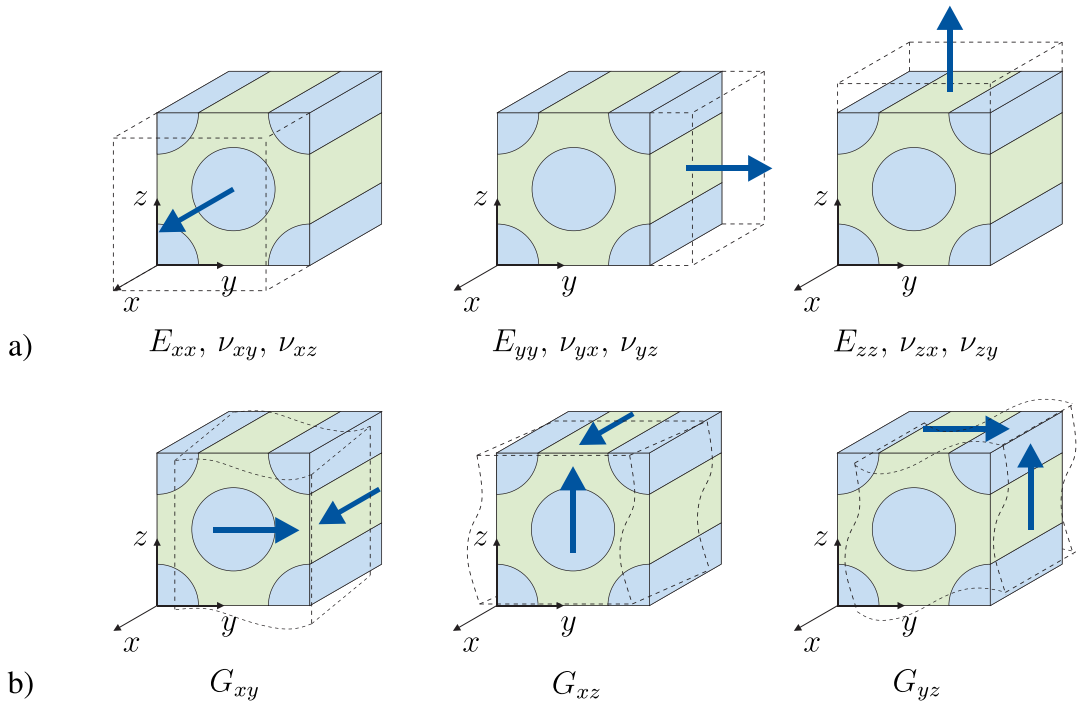

Fig. 11. Schematic representation of the boundary conditions in terms of the six uniaxial strain states for deriving the effective elastic material properties. (a) Monotonic, uniaxial tension (b) Pure shear.

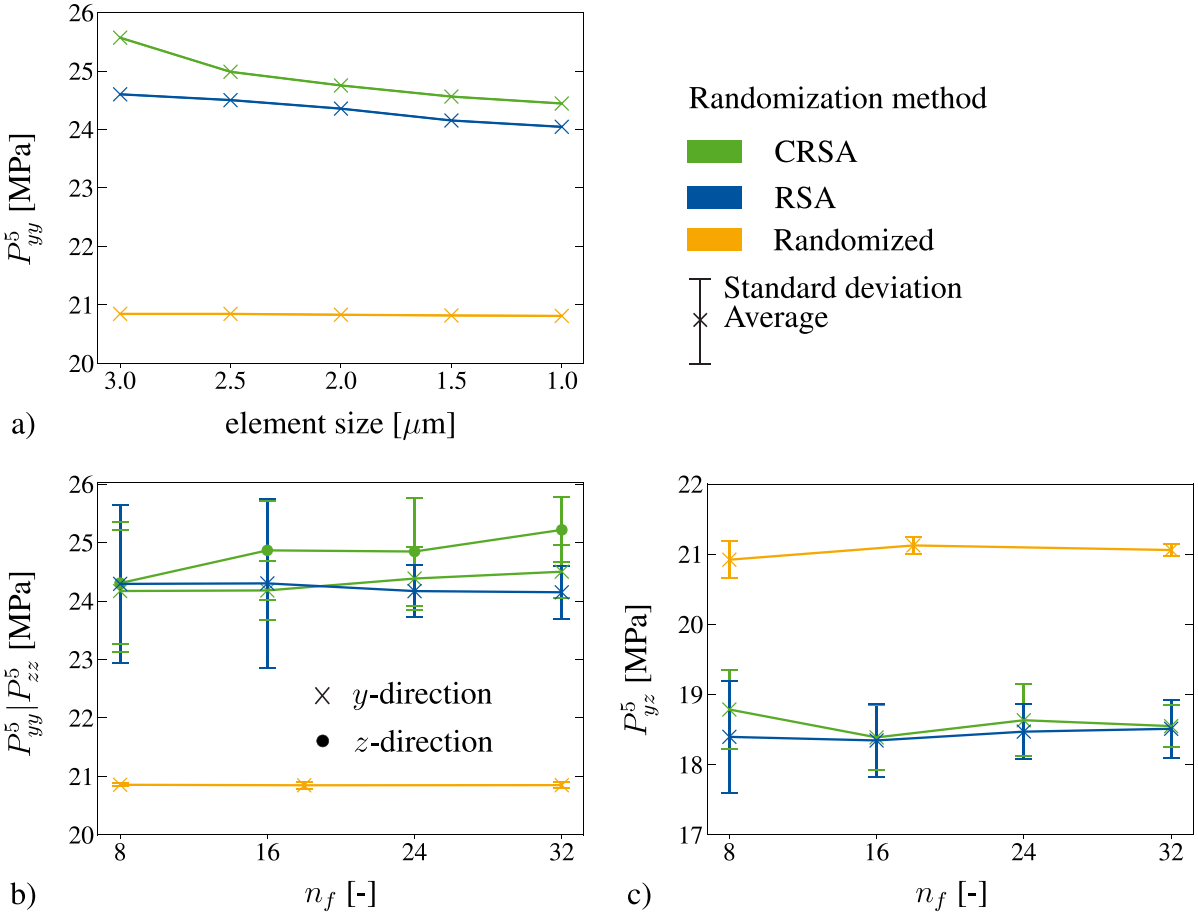

Fig. 12. (a) Mesh convergence study (b) Size convergence study: Tension in y-direction (Standard deviation indicated by the error bars) (c) Size convergence study: Pure shear in yz-direction (Standard deviation indicated by the error bars). For the corresponding periodic boundary conditions, the reader is referred to Fig. 11. P^5_* indicates the engineering stress (1. Piola–Kirchhoff stress) at 5% strain.

clustering. In contrast to the RSA based methods, the material response in y-direction is less stiff for the randomized method, whereas in the case of pure shear, the stiffest material response is present. Thus, a direct correlation between the amount of fiber clustering and the overall in-plane material response can be drawn, where a higher amount of clustering generally leads to a higher difference between tensile and shear behavior.

In terms of the convergence criterion, the deviation to the previous realization is adopted as previously done for the mesh convergence study. Consequently, $n_f = 18$ can be regarded as the converged RUC size for the randomized method. Compared to the randomized method, the RSA and the CRSA method show pronounced differences between the shear and tensile response. Here, the CRSA method results in a slightly stiffer material behavior, especially in the tensile load case. In general, the standard deviation decreases with increasing RUC size and similar to the mesh convergence study, the amount of fiber clustering influences the convergence rate. At 24 fibers, convergence is reached for the RSA method, whereas 32 fibers are needed for the clustered RSA method in z-direction. Interestingly enough, in y-direction convergence for the CRSA is already reached for 24 fibers. Additionally, in this direction, the unit cell response is similar to the RSA method. In the following, $n_f = 32$ is chosen for all unit cells as the common denominator.

5. Unit cell identification and validation against experimental results

5.1. Parameter identification

In Reuvers et al. (2024), the thermomechanically coupled matrix model for polyamide 6 was developed, characterized and validated with mechanical and thermal experimental data. Therefore, a staggered parameter identification procedure was used on the isothermal model to obtain a set of mechanical and thermal material parameters for each test temperature. Here, a novel blending technique of the polymer PA6 together with cyclic olefin copolymer (COC) during specimen production allowed testing on a broad variety of stable DOCs. The resulting material model is valid for DOCs between 15% and 29%. In the following, a brief overview of the identification scheme is given:

1. The total Young's modulus E_{tot} was obtained from the initial slope of the true stress–strain relations for different DOCs. Next, the exponential dependence of the Young's modulus on the crystallinity was found using nonlinear regression. In contrast to the Young's modulus, the Poisson's ratio calculated via the negative ratio of the measured transverse and longitudinal strain, showed no clear dependence on the DOC. Hence, it was chosen as a constant ν_{tot}.
2. Based on a post-processing scheme introduced by Amin et al. (2006), uniaxial long-term relaxation tests at various strain states revealed a nonlinear dependence of the relaxation time τ on the visco-elastic overstress $\boldsymbol{\tau}_2$ and the corresponding strain state represented by the visco-elastic right Cauchy–Green tensor $\boldsymbol{C}_v$ (see Fig. 13). Similar to the Poisson's ratio, no clear dependence on the DOC was visible, in line with the assumption of the visco-elastic part corresponding mainly to the amorphous response of the material. For the relaxation time, the power-law-type function $\tau = \tau_0 \|\boldsymbol{B}_v\|^{\gamma} \exp(-\delta \|\boldsymbol{\tau}_2\|)$ was chosen. Here, a dependence on the visco-elastic left Cauchy–Green tensor $\boldsymbol{B}_v = \boldsymbol{F}_v \boldsymbol{F}_v^T$ and the Kirchhoff overstress $\boldsymbol{\tau}_2$ was introduced. The temperature dependent material parameters $\tau_0(\theta), \gamma(\theta)$ and $\delta(\theta)$ were identified using nonlinear curve fitting.
3. Above room temperature, it was not possible to directly obtain the yield stress in tension σ_t^0 and compression σ_c^0 from monotonic or cyclic tension and compression test. Hence, these material parameters together with the parameters related to nonlinear Armstrong–Frederick hardening (b, c) were identified using a nonlinear multiple curve fitting procedure. Firstly, the ideal parameters for each DOC were governed using a single fit independent of the crystallinity. Next, the results for each parameter were plotted over the DOC and a linear trend line was identified using a multi curve fit. In this way, the dependence on the DOC was found and incorporated into the model for each test temperature.
4. Finally, the parameters related to the thermal characteristics of the model as the conductivity λ_t, specific heat capacity c_T, the thermal expansion coefficient α_T and the density ρ_0 were determined experimentally. Similar to the Young's modulus, a dependence on the DOC was found using linear regression.

Table 4
Mechanical matrix material parameters for $\chi = 0.41$ at all test temperatures.

Parameter		23 °C	100 °C	150 °C
E_{tot}	[MPa]	3800	832.0	484.89
ν_{tot}	[–]	0.35	0.45	0.45
σ_t^0	[MPa]	25.0	2.6	2.51
c	[MPa]	17.756	162.39	171.25
b	[MPa]	1.276	147.445	158.90
$\tau = \tau_0(\theta) \|\|\boldsymbol{B}_v\|\|^{\gamma(\theta)} \exp(-\delta(\theta) \|\|\boldsymbol{\tau}_2\|\|)$	τ_0 [s]	1853.653	1035.238	573.899
	γ [–]	4.57	4.3	4.289
	δ [–]	0.539	0.759	0.873

Table 5
Mechanical and thermal glass fiber material parameters.

E_{fiber} [GPa]	ν_{fiber} [–]	$\alpha_{T,\text{fiber}}$ [10^{-6}/K]	$c_{T,\text{fiber}}$ [J/g K]	$\lambda_{T,\text{fiber}}$ [W/m K]	$\rho_{0,\text{fiber}}$ [g/cm^3]
73	0.22	5.0	803	1.35	2.58

The complete set of mechanical and thermal parameters for the matrix material model up to a DOC of 29% is provided in Tables 8 and 9 in Appendix. In the current work, the DSC results of the composite material revealed a DOC of $\chi \approx 0.41$ (cf. Section 2), which is beyond the identified parameter range. The extrapolated parameters from Tables 8 and 9 were tested for their suitability and compared to the experimental results from Section 2, however, only the thermal parameters as well as the crystallinity independent parameters for the visco-elastic branch were suitable. In Reuvers et al. (2024), DIC was used only for the visco-elastic tests to exploit the post-processing procedure by Amin et al. (2006). All other test results were converted to true stress and strain results under the assumption of incompressibility. Hence, it is reasonable that extrapolated values from these results do not correspond to the current experimental data, which was obtained using DIC in all test cases. To obtain suitable parameters for the Young's modulus, the yield stress as well as the two hardening parameters, nonlinear curve fitting was used. Due to the lack of compression data above room temperature, the tension–compression asymmetry in yielding was neglected ($m = 1.0$). An overview of the mechanical parameters for a DOC of $\chi \approx 0.41$ is presented in Table 4. For the glass fibers, the temperature independent parameters were supplied by the manufacturer and can be found in Table 5.

5.2. Comparison of RUC and experimental results as well as further numerical calculations

Mechanical results

In order to derive the effective mechanical material properties and compare the results to the experimental findings from Section 2, the six uniaxial strain states (see Fig. 11) are applied successively on the RUCs. For each randomization method, 10 different RUCs are evaluated under isothermal conditions. The averaged results are shown in Table 6 for the

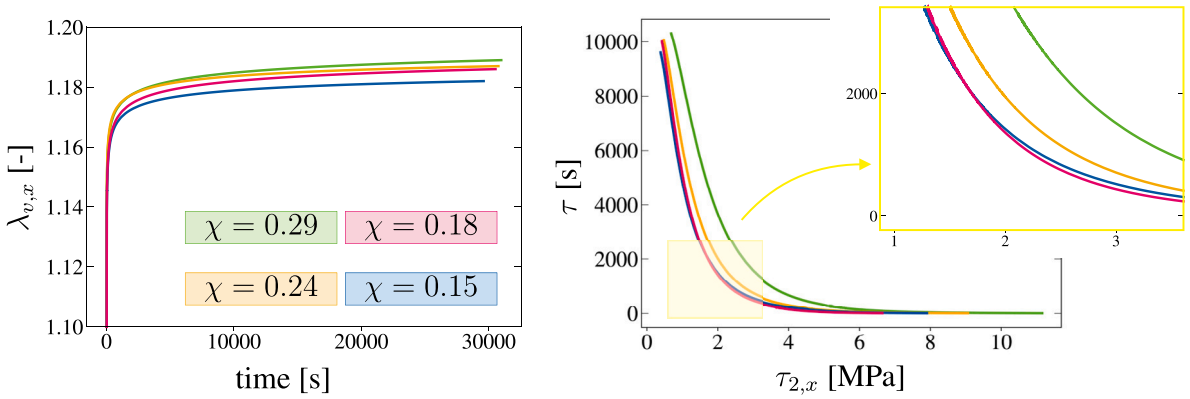

Fig. 13. Results of the visco-elastic post-processing procedure from Reuvers et al. (2024): Inelastic stretch over time and relaxation time over Kirchhoff stress for an exemplary temperature of 100 °C and various DOCs χ.

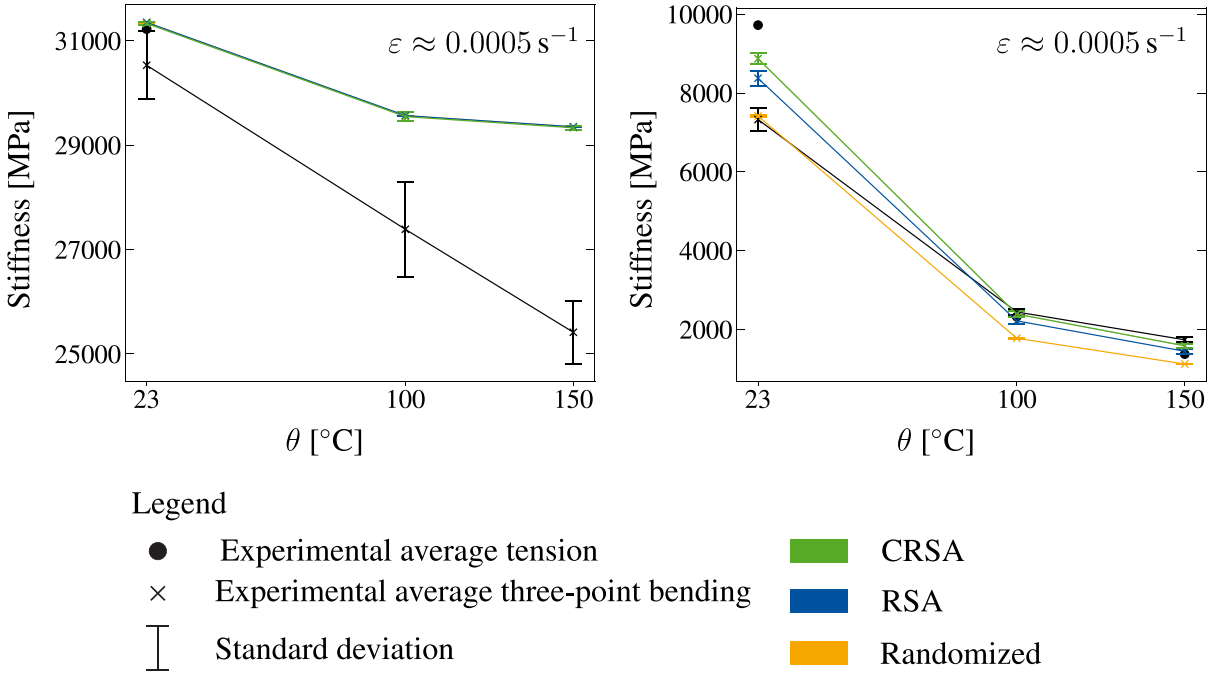

Fig. 14. Comparison of experimental and simulative material stiffness in x- and y-direction for various temperatures and randomization methods.

three test temperatures together with the standard deviation s. Generally, the material stiffness tensor of transverse isotropic materials is defined by the following five material parameters: $E_{xx}, E_{yy}, \nu_{xy}, G_{xy}, G_{yz}$, where the symmetry between y- and z-direction is already exploited. This symmetry is, however, weakened for the CRSA method, where a high degree of clustering in z–direction leads to differences in the in-plane material characteristics. Consequently, the resulting material behavior from the CRSA method is orthotropic and defined by the following nine material constants: $E_{xx}, E_{yy}, E_{zz}, \nu_{xy}, \nu_{xz}, \nu_{yz}, G_{xy}, G_{xz}, G_{yz}$. In Table 6, all nine material constants are presented for completeness, even though in the case of the randomized or RSA method the material constants are reduced to six. As expected, the material stiffness in x-direction is higher compared to the stiffness in y- and z-direction due to the dominant fiber influence. Moreover, the dependence on the temperature is least pronounced in fiber direction, which corresponds to the finding of Gröger et al. (2021) and the three-point-bending tests in Section 2. A more detailed overview of the reduction in material stiffness with increasing temperature is presented in Fig. 14, where the experimental material stiffness from tensile and three-point-bending tests are compared to the simulative results. The simulative results at room temperature are in good agreement with the experimental data. Above the glass transition, the predicted material stiffness in fiber direction deviates from the tensile response as expected due to the 2D measurement error discussed in Section 2. Interestingly enough, the temperature dependence in x-direction is more pronounced for the results of the bending tests compared to the RUC results and findings from (Gröger et al., 2021). The authors suspect that this softening might be related to delamination effects at the interface between fibers and matrix, which could be confirmed by a microscopic examination of the test specimens directly after testing or DIC measurements during testing. Another possibility could be a reduction in stiffness of the glass fibers resulting from the temperature increase. For example in Jenkins et al. (2015) a reduction in fiber stiffness was reported after thermal conditioning for 25 min at 200 °C, suggesting that the stiffness

Table 6
Effective elastic material parameters for various material directions and randomization methods at temperatures below and above the glass transition. The standard deviation is indicated by s.

$n = 10$	Randomization method	E_{xx} [MPa]	E_{yy} [MPa]	E_{zz} [MPa]	ν_{xy} [–]	ν_{xz} [–]	ν_{yz} [–]	G_{xy} [MPa]	G_{zx} [MPa]	G_{yz} [MPa]
23 °C	Randomized	31 350.23	7417.33	7460.11	0.29	0.29	0.50	45.50	44.99	6651.27
s		0.249	21.651	27.396	0.0003	0.0003	0.002	0.153	0.133	24.391
	RSA	31 352.74	8374.29	8388.99	0.29	0.29	0.44	46.31	46.46	5847.62
s		0.345	188.741	154.343	0.006	0.006	0.011	0.615	0.804	148.625
	CRSA	31 332.06	8871.82	8463.88	0.29	0.29	0.43	44.59	49.06	5667.99
s		34.717	131.550	104.993	0.001	0.001	0.010	0.367	0.622	79.094
100 °C	Randomized	29 563.95	1776.92	1779.63	0.35	0.35	0.78	9.78	9.94	1465.10
s		0.259	6.280	6.697	0.0007	0.0007	0.002	0.027	0.036	10.883
	RSA	29 567.14	2219.74	2223.35	0.35	0.35	0.72	10.19	10.21	1236.72
s		0.485	84.704	80.705	0.004	0.004	0.012	0.206	0.147	52.849
	CRSA	29 547.14	2390.97	2350.33	0.34	0.36	0.71	10.94	9.72	1171.88
s		33.877	76.597	70.923	0.003	0.003	0.010	0.175	0.096	26.188
150 °C	Randomized	29 351.08	1123.51	1127.57	0.35	0.35	0.79	5.76	5.85	1020.05
s		0.232	5.794	6.465	0.0007	0.0007	0.002	0.016	0.022	7.690
	RSA	29 353.08	1447.69	1450.47	0.35	0.35	0.73	6.01	6.02	835.92
s		0.365	62.314	58.262	0.004	0.004	0.012	0.125	0.089	39.207
	CRSA	29 332.82	1584.72	1538.37	0.34	0.36	0.72	6.46	5.72	791.60
s		33.817	54.129	48.874	0.003	0.003	0.010	0.106	0.058	19.882

decreased already between room and elevated temperatures. Hereby, the thermal conditioning time is similar to the heating phase for the experiments in Section 2. This decrease in fiber stiffness is, however, not accounted for in the RUC simulations (cf. Table 5) due to the lack of data from the manufacturer.

As indicated in Table 6, the material stiffness in y- and z-direction as well as the shear moduli G_{xy} and G_{zx} show no significant deviation for the randomization and the RSA method. The high degree of fiber clustering in the CRSA method, however, leads to pronounced differences at room temperature that are negligible above the glass transition.

The Poisson's ratios ν_{xy} and ν_{xz} correspond well with the experimental findings from Section 2 above the glass transition. However, at room temperature, the RUC results show an increased lateral contraction compared to the experimental results. Interestingly enough, below the glass transition, the Poisson's ratios ν_{xy} and ν_{xz} are independent of the randomization method, and the differences at higher temperatures are only minor. In terms of the standard deviation, the results correspond with those of the convergence studies in Section 4, where the standard deviation of the randomized method is smaller compared to the RSA and CRSA methods. This finding translates to the stress fields for an exemplary temperature of 100 °C in Fig. 15 and $\epsilon = 0.25$, where the randomized method shows the most homogeneous stress distribution in all directions. Hereby, stress peaks are mainly visible in regions with increased fiber clustering. This phenomenon is particularly evident in the CRSA method, where slight band formation is also visible in the yy- and xy-directions. In fiber direction, no significant differences between the stress fields of all randomization methods are present in line with the results for the material stiffness E_{xx} in Table 6. Here, the fibers are the load bearing component, as indicated by the stress field.

A detailed comparison of experimental and simulative results beyond the elastic material regime is presented in Fig. 16 for the material response perpendicular to the fibers at all respective test temperatures. The results for the RSA and CRSA method are in good agreement with the experimental data, whereas the randomized method yields a softer material response similar to the convergence study results from Section 4. Consequently, the authors conclude that both the RSA and the CRSA method are eligible for the present material. For a further selection, additional tests, such as for example, shear tests or a detailed microscopic examination of the underlying fiber distribution beyond the investigations in Section 2 would be necessary, which was, however, beyond the scope of this work. Nonetheless, both RSA and CRSA method yield valid results in comparison to the experiments and can be used to generate a data basis for the identification of the macroscopic material model.

Table 7
Effective thermal conductivity for various material directions and randomization methods (s denotes the standard deviation). $\lambda_{xy} = \lambda_{yx} = \lambda_{xz} = \lambda_{zx} = \lambda_{yz} = \lambda_{zy} \approx 0$.

n = 10	Randomization method	λ_{xx} [W/m K]	λ_{yy} [W/m K]	λ_{zz} [W/m K]
	Randomized	0.7991	0.5919	0.5894
s		0.0015	0.0009	0.0008
	RSA	0.8040	0.5947	0.5944
s		0.0028	0.0033	0.0035
	CRSA	0.8022	0.5840	0.6073
s		0.0042	0.0028	0.0026

Thermal results

To determine the effective thermal conductivity tensor from the averaged heat flux over the RUC domain a series of $n = 10$ tests is performed for each randomization method. Therefore, a temperature difference $\Delta T = 1$ K is successively applied in x-, y- and z-direction under steady-state heat transfer conditions as stated in Section 4. In Reuvers et al. (2024), the conductivity of the polyamide 6 matrix was found to be dependent on the degree of crystallinity, however, the temperature influence was negligibly small (cf. Table 9). For the conductivity of the glass fibers no temperature influence is reported by the manufacturer in the considered temperature range. Consequently, the effective thermal conductivity tensor of the composite is derived only at room temperature. The results of the computations are given in Table 7 as the mean value together with the standard deviation s. For all computations, the off-diagonal entries of the thermal conductivity tensor were four or more orders of magnitude smaller than the entries on the main diagonal and are, thus, considered as null $\lambda_{xy} = \lambda_{yx} = \lambda_{xz} = \lambda_{zx} = \lambda_{yz} = \lambda_{zy} \approx 0$. Hence, only the conductivities in x-, y- and z-direction are presented.

Similar to the mechanical results, the in-ply conductivities for the randomized and RSA methods are approximately equal, with the randomized method having the lowest standard deviation. For the CRSA method, the thermal conductivity in z-direction is higher compared to the conductivity in y-direction, which can be attributed to the higher degree of clustering resulting in a layered structure. Generally, all results in y- and z-direction correspond well with the experimentally determined values in z-direction of 0.5889 W/m K for 23° and 0.6365 W/m K as the median over all test temperatures (cf. Fig. 7). In fiber direction, the thermal conductivity is fiber dominated and, thus, higher compared to the in-ply results for all randomization methods. Interestingly enough, the anisotropic thermal conductivity is not

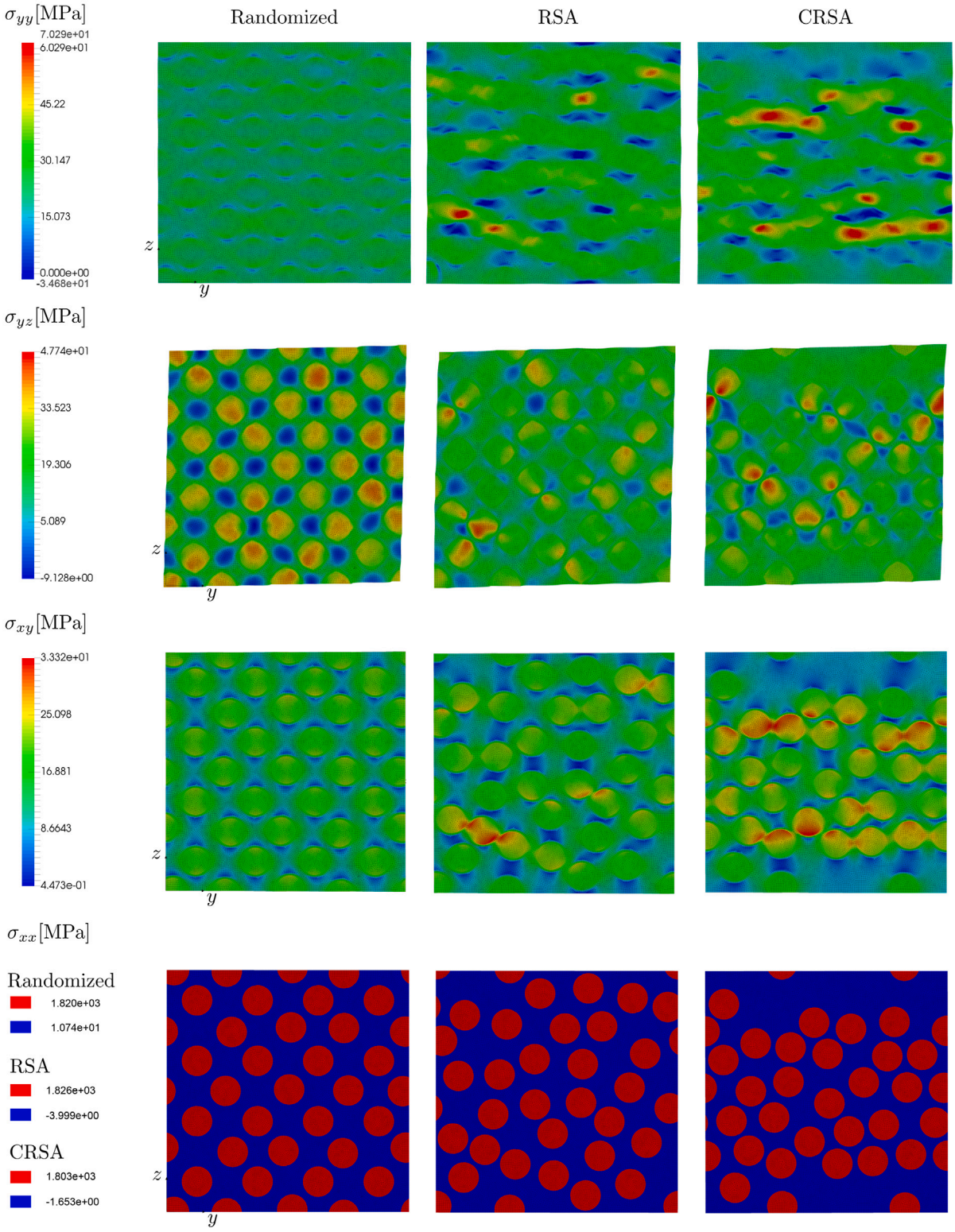

Fig. 15. Exemplary in-plane stress fields (Cauchy stress) for all three randomization methods at $\varepsilon = 0.025$ and 100 °C after application of the far field strains in the corresponding material directions.

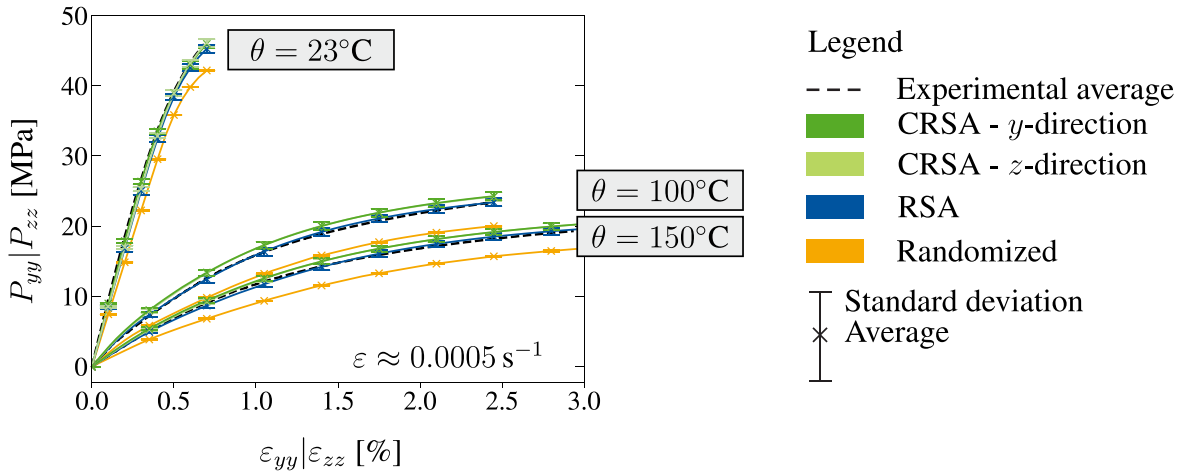

Fig. 16. Comparison of experimental and simulative results perpendicular to the fiber direction for various temperatures and randomization methods.

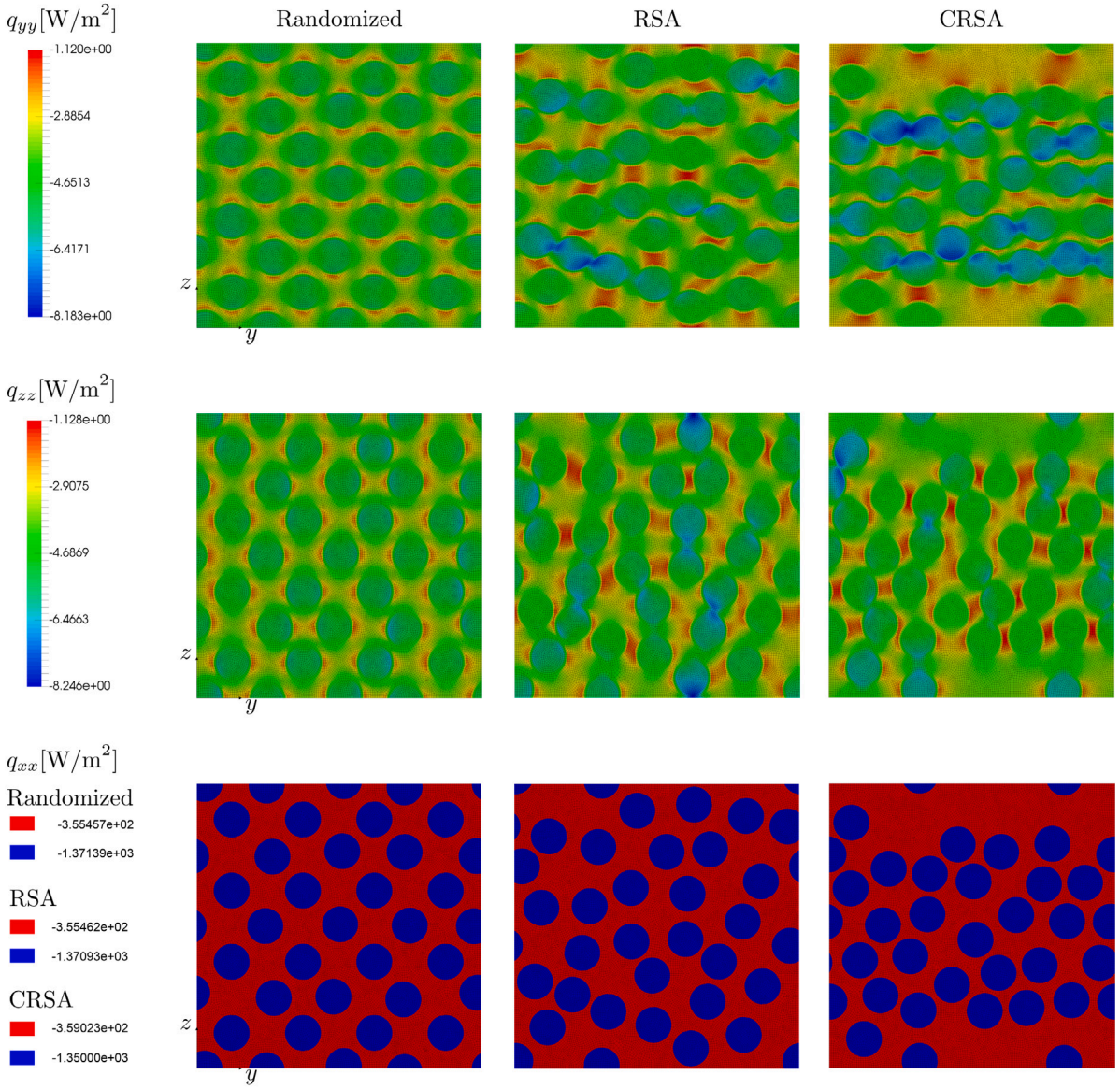

Fig. 17. In-plane heat flux field for all three randomization methods after application of a 1 K temperature difference in x-, y- and z-direction.

material-induced but rather geometry induced since both material constituents are thermally isotropic on their own. To give an insight on local differences between the randomization methods, exemplary heat flux fields resulting from the application of a temperature difference in x-, y- and z-direction are shown in Fig. 17. Here, the in-ply heat flux field of the randomized method is the most homogeneous, whereas directional dependencies can clearly be indicated for the RSA and CRSA method. Slight band formation is visible for the RSA and CRSA method in y- and z-direction throughout all realizations, however, most pronounced for the heat flux of the CRSA RUC in y-direction, resulting from the high degree of fiber clustering. In x-direction, the heat flux fields of all randomization methods show no significant differences, consistent with the findings in Table 7.

6. Conclusion and outlook

In this work, a computational micromechanics framework was presented, incorporating thermal and mechanical effects on the microscale to predict the homogenized material behavior of an experimentally tested glass fiber reinforced polyamide 6 single ply. To this end, monotonic and cyclic experimental tests were conducted in various material directions, e.g. tension, compression and bending, including testing at various temperatures and strain rates. The results showed the materials' direction dependency due to the unidirectional reinforcement and confirmed the temperature and strain rate dependency mainly perpendicular to the fibers, where the polyamide 6 material dominates the material response. Additional tensile tests under varying fiber angle displayed the nonlinear influence of the fiber angle on the composite material behavior. Furthermore, the material was thermally characterized, including a TMA, DSC and *Hot-Disk* measurements indicating a temperature influence on the thermal material parameters. Next, a thermomechanically coupled material model formulation for the PA6 matrix was summarized that captures the nonlinear visco-elastic, elasto-plastic material behavior, incorporating the Bauschinger effect via nonlinear kinematic hardening together with a tension–compression asymmetry in yielding. The degree of crystallinity enters the constitutive equations as a constant input quantity to account for the effect of the underlying material morphology on the overall material behavior, as well as the interplay between the biphasic matrix microstructure and applied thermal conditions. In Reuvers et al. (2024), the model formulation was already identified for polyamide 6 blends for a range of DOCs between 15 and 29% and extended up to 41% in this contribution with the presented experimental results. Together with an elastic material model for the glass fibers, the presented matrix model formulation was used in the context of repeating unit cell simulations. Therefore, various randomization methods were tested during the generation of the unit cells to predict the random fiber distribution. Here, the focus lied on process automation. Consequently, a plug-in was developed using the Abaqus–Python interface. In the following, a statistical investigation, where the Hill–Mandel condition was exploited to obtain homogenized mechanical and thermal results indicated the necessary mesh and unit cell size to achieve converged results. The comparison of experimental and numerical mechanical and thermal results showed a strong agreement and confirmed the applicability of the repeating unit cells. In terms of the mechanical results, the RSA and CRSA methods were found to reflect the material behavior best, whereas the effect of the randomization method ,for example, on the effective thermal parameters was negligible. In general, the authors would recommend to use the CRSA method, which showed to be more accurate regarding the production induced orthotropic material behavior and the visual comparison with the microscopic images. Moreover, the high amount of fiber clustering might be able to reproduce delamination phenomena if damage effects were incorporated in the matrix material. In the present case, however, the small plate thickness limited completing the mechanical and thermal experimental study for all three material directions. Thus, the RSA method provides a simpler solution, with the reduction from orthotropic to transversely isotropic material behavior. In the future, the established and experimentally validated unit cells will be used for the development of a broad data basis for the single ply response of glass fiber reinforced polyamide 6, enabling testing on additional temperatures and strain rates. Furthermore, previously unseen loading conditions, as for example shear, can be examined without the accompanying experimental effort. The concept can also be adjusted to cater for altered material design, as for example, using a different fiber volume content or exchanging the underlying material constituents, given that the knowledge of their individual material behavior is known. This data basis will then be used in an upcoming publication to identify a homogenized macroscopic material model, accounting for the underlying micro-thermomechanical effects through the presented framework. The macromodel will be tested in the context of thermoforming simulations to demonstrate the enhancements made through the inclusion of the crystallinity dependence and the thermo-mechanical coupling in the formulation.

CRediT authorship contribution statement

Marie-Christine Reuvers: Writing – review & editing, Writing – original draft, Visualization, Validation, Software, Methodology, Investigation, Formal analysis, Data curation, Conceptualization. **Christopher Dannenberg:** Visualization, Software, Investigation, Formal analysis. **Sameer Kulkarni:** Methodology, Investigation, Data curation. **Klara Loos:** Writing – review & editing, Supervision. **Michael Johlitz:** Conceptualization, Funding acquisition, Supervision, Writing – review & editing. **Alexander Lion:** Conceptualization, Funding acquisition, Supervision, Writing – review & editing. **Stefanie Reese:** Writing – review & editing, Supervision, Funding acquisition, Conceptualization. **Tim Brepols:** Writing – review & editing, Supervision, Conceptualization.

Declaration of competing interest

The authors declare the following financial interests/personal relationships which may be considered as potential competing interests: Marie-Christine Reuvers reports financial support was provided by German Research Foundation. Sameer Kulkarni reports financial support was provided by German Research Foundation. Michael Johlitz reports financial support was provided by German Research Foundation. Alexander Lion reports financial support was provided by German Research Foundation. Stefanie Reese reports financial support was provided by German Research Foundation. Tim Brepols reports financial support was provided by German Research Foundation. If there are other authors, they declare that they have no known competing financial interests or personal relationships that could have appeared to influence the work reported in this paper.

Data availability

Data will be made available on request.

Acknowledgments

The author gratefully acknowledges the DSC results conducted by Dr. André Wutzler at the Polymer Service GmbH (PSM) Merseburg. Furthermore, financial support by the German Research Foundation (DFG) (RE 1057/52-1, project number 454873500) is gratefully acknowledged.

Appendix

A.1. Mechanical and thermal material parameters for the polyamide 6 matrix model

See Tables 8 and 9.

Table 8
Set of mechanical material parameters at different temperatures for a range of DOC between 15 and 29% from Reuvers et al. (2024).

Function	Parameter at:	23 °C	50 °C	100 °C	130 °C	150 °C
$E_{tot}(\chi) = C_1(\theta)\exp(C_2(\theta)\chi)$	C_1 [MPa]	2397	2270[a]	143.1	96.875	102.1
$E_2 = E_{tot} - E_1$	C_2 [–]	0.9106	−0.8716[a]	5.133	5.565	5.373
$E_1 = m_E(\chi)E_{tot}$	m_E [–]					
$m_E = 1.07143\chi + 0.38935$						
$\nu_{tot}(\theta) = \nu_1 = \nu_2$	[–]	0.35	0.45	0.45	0.45	0.45
$\sigma_c^0 = c_1(\theta)\chi + c_2(\theta)$	c_1 [MPa]	72.19	138.8	26.95	20.86	13.19
	c_2 [MPa]	41.96	−21.913	−3.192	−2.969	−1.436
$\sigma_t^0 = c_3(\theta)\chi + c_4(\theta)$	c_3 [MPa]	72.19	131.24	25.38	20.27	12.93
	c_4 [MPa]	41.96	−20.984	−3.006	−2.884	−1.407
$c = c_5(\theta)\chi + c_6(\theta)$	c_5 [MPa]	$c = 17.756$[b]	20.86	834.5	597.3	523.8
	c_6 [MPa]		92.213	−94.56	−69.42	−67.89
$b = c_7(\theta)\chi + c_8(\theta)$	c_7 [–]	$b = 1.276$[b]	0	355.4	150.2	196.3
	c_8 [–]		60.438	−53.15	−22.39	−28.3
$\tau = \tau_0(\theta)\,\|\|\boldsymbol{B}_v\|\|^{\gamma(\theta)}\exp(-\delta(\theta)\,\|\|\boldsymbol{\tau}_2\|\|)$	τ_0 [s]	1853.653	1511.952	1035.238	737.245	573.899
	γ [–]	4.57	4.416	4.3	4.872	4.289
	δ [–]	0.539	0.814	0.759	0.866	0.873

[a] Inconsistent results due to testing in the glass transition regime.

[b] Constant values obtained for $\chi = 0.29$ only, due to early failure of the remaining blends.

Remark: The reader is kindly reminded, that although some coefficients of the identified functions determining the material parameters, are negative, the material parameters themselves are always positive for the range of DOCs ($\chi = 0.15 - 0.29$) the model spans.

Table 9
Set of thermal material parameters at different temperatures from Reuvers et al. (2024).

Function	Parameter at:	23 °C	50 °C	100 °C	130 °C	150 °C
$\alpha_T(\chi) = c_9(\theta)\chi + c_{10}(\theta)$	c_9 [10^{-4}/K]	−0.2601	−0.3586	−5.857	−3.336	−2.238
	c_{10} [10^{-4}/K]	0.8756	1.218	3.122	2.565	2.431
$c_T(\chi) = c_{11}(\theta)\theta + c_{12}(\theta)$	c_{11} [J/g K]	0.00471	0.00401	0.00401	0.00401	0.00401
	c_{12} [J/g K]	1.25313	1.52299	1.52299	1.52299	1.52299
$\lambda_T(\chi) = c_{13}\chi + c_{14}$	c_{13} [W/m K]	0.4338	0.4338	0.4338	0.4338	0.4338
	c_{14} [W/m K]	0.1855	0.1855	0.1855	0.1855	0.1855
$\rho_0(\chi) = c_{15}\chi + c_{16}$	c_{15} [g/mm^3]	0.4878	0.4878	0.4878	0.4878	0.4878
	c_{16} [g/mm^3]	0.9897	0.9897	0.9897	0.9897	0.9897

Remark: The reader is kindly reminded, that although some coefficients of the identified functions determining the material parameters, are negative, the material parameters themselves are always positive for the range of DOCs ($\chi = 0.15 - 0.29$) the model spans.

References

Amin, A., Lion, A., Sekita, S., Okui, Y., 2006. Nonlinear dependence of viscosity in modeling the rate-dependent response of natural and high damping rubbers in compression and shear: Experimental identification and numerical verification. Int. J. Plast. 22 (9), 1610–1657.

Armstrong, P.J., Frederick, C., et al., 1966. A Mathematical Representation of the Multiaxial Bauschinger Effect. In: CEGB Report RD/B/N731, vol. 731, Central Electricity Generating Board and Berkeley Nuclear Laboratories, Research & Development Department.

Ayoub, G., Zaïri, F., Fréderix, C., Gloaguen, J.-M., Naït-Abdelaziz, M., Seguela, R., Lefebvre, J.-M., 2011. Effects of crystal content on the mechanical behaviour of polyethylene under finite strains: Experiments and constitutive modelling. Int. J. Plast. 27 (4), 492–511.

Bargmann, S., Klusemann, B., Markmann, J., Schnabel, J., Schneider, K., Soyarslan, C., Wilmers, J., 2018. Generation of 3d representative volume elements for heterogeneous materials: A review. Prog. Mater. Sci. 96, 322–384.

Campoy, I., Gomez, M.A., Marco, C., 1998. Structure and thermal properties of blends of nylon 6 and a liquid crystal copolyester. Polymer 39 (25), 6279–6288.

Daniel, I., Luo, J.-J., Schubel, P., Werner, B., 2009. Interfiber/interlaminar failure of composites under multi-axial states of stress. Compos. Sci. Technol. 69 (6), 764–771.

Dettmer, W., Reese, S., 2004. On the theoretical and numerical modelling of Armstrong-Frederick kinematic hardening in the finite strain regime. Comput. Methods Appl. Mech. Engrg. 193 (1–2), 87–116.

Eckart, C., 1948. The thermodynamics of irreversible processes. IV. The theory of elasticity and anelasticity. Phys. Rev. 73 (4), 373.

Feder, J., 1980. Random sequential adsorption. J. Theoret. Biol. 87 (2), 237–254.

Felder, S., Holthusen, H., Hesseler, S., Pohlkemper, F., Gries, T., Simon, J.-W., Reese, S., 2020a. Incorporating crystallinity distributions into a thermo-mechanically coupled constitutive model for semi-crystalline polymers. Int. J. Plast. 135, 102751.

Felder, S., Kopic-Osmanovic, N., Holthusen, H., Brepols, T., Reese, S., 2022. Thermo-mechanically coupled gradient-extended damage-plasticity modeling of metallic materials at finite strains. Int. J. Plast. 148, 103142.

Felder, S., Vu, N.A., Reese, S., Simon, J.-W., 2020b. Modeling the effect of temperature and degree of crystallinity on the mechanical response of polyamide 6. Mech. Mater. 148, 103476.

Feyel, F., Chaboche, J.-L., 2000. Fe2 multiscale approach for modelling the elastovisco-plastic behaviour of long fibre sic/ti composite materials. Comput. Methods Appl. Mech. Engrg. 183 (3–4), 309–330.

Geers, M., Kouznetsova, V., Brekelmans, W., 2010. Multi-scale computational homogenization: Trends and challenges. J. Comput. Appl. Math. 234 (7), 2175–2182.

Ghorbel, E., 2008. A viscoplastic constitutive model for polymeric materials. Int. J. Plast. 24 (11), 2032–2058.

Gierden, C., Kochmann, J., Waimann, J., Svendsen, B., Reese, S., 2022. A review of FE-FFT-based two-scale methods for computational modeling of microstructure evolution and macroscopic material behavior. Arch. Comput. Methods Eng. 29 (6), 4115–4135.

Gröger, B., Hornig, A., Hoog, A., Gude, M., 2021. Temperature dependent modelling of fibre-reinforced thermoplastic organo-sheet material for forming and joining process simulations. Key Eng. Mater. 883, 49–56.

Hadipeykani, M., Aghadavoudi, F., Toghraie, D., 2020. A molecular dynamics simulation of the glass transition temperature and volumetric thermal expansion coefficient of thermoset polymer based epoxy nanocomposite reinforced by CNT: a statistical study. Phys. A 546, 123995.

Herráez, M., González, C., Lopes, C., De Villoria, R.G., LLorca, J., Varela, T., Sánchez, J., 2016. Computational micromechanics evaluation of the effect of fibre shape on the transverse strength of unidirectional composites: an approach to virtual materials design. Composites A 91, 484–492.

Hill, R., 1963. Elastic properties of reinforced solids: some theoretical principles. J. Mech. Phys. Solids 11 (5), 357–372.

Hill, R., 1967. The essential structure of constitutive laws for metal composites and polycrystals. J. Mech. Phys. Solids 15 (2), 79–95.

Hine, P., Lusti, H., Gusev, A., 2002. Numerical simulation of the effects of volume fraction, aspect ratio and fibre length distribution on the elastic and thermoelastic properties of short fibre composites. Compos. Sci. Technol. 62 (10–11), 1445–1453.

Hinrichsen, E., Feder, J., Jøssang, T., 1986. Geometry of random sequential adsorption. J. Stat. Phys. 44, 793–827.

Hinton, M., Kaddour, A., Soden, P., 2004. A further assessment of the predictive capabilities of current failure theories for composite laminates: comparison with experimental evidence. Compos. Sci. Technol. 64 (3–4), 549–588.

Holmes, D., Loughran, J., Suehrcke, H., 2006. Constitutive model for large strain deformation of semicrystalline polymers. Mech. Time-Depend. Mater. 10, 281–313.

Jenkins, P., Yang, L., Liggat, J., Thomason, J., 2015. Investigation of the strength loss of glass fibre after thermal conditioning. J. Mater. Sci. 50, 1050–1057.
Kalaprasad, G., Pradeep, P., Mathew, G., Pavithran, C., Thomas, S., 2000. Thermal conductivity and thermal diffusivity analyses of low-density polyethylene composites reinforced with sisal, glass and intimately mixed sisal/glass fibres. Compos. Sci. Technol. 60 (16), 2967–2977.
Kanit, T., Forest, S., Galliet, I., Mounoury, V., Jeulin, D., 2003. Determination of the size of the representative volume element for random composites: statistical and numerical approach. Int. J. Solids Struct. 40 (13–14), 3647–3679.
Kröner, E., 1959. Allgemeine kontinuumstheorie der versetzungen und eigenspannungen. Arch. Ration. Mech. Anal. 4, 273–334.
Kugele, D., 2020. Experimentelle und numerische untersuchung des abkühlverhaltens thermoplastischer gelegelaminate in der prozesskette.
Kulkarni, S., Loos, K., Lion, A., Johlitz, M., 2022. Thermoforming: Identification of Process-Relevant Ranges for Strain, Strain Rate, Cooling Rate, and Degree of Crystallinity Through Preliminary Simulations. In: Lectures Notes on Advanced Structured Materials, Springer, pp. 303–314.
Kulkarni, S., Reuvers, M.-C., Brepols, T., Reese, S., Johlitz, M., Lion, A., 2023. Characterization of crystallization kinetics in polyamide 6 with a focus on modeling the thermoforming process: experiments, modeling, simulations. Contin. Mech. Thermodyn. 1–17.
Lee, E., 1969. Elastic–plastic deformation at finite strains. J. Appl. Mech. 36 (1), 1–6.
Li, J., Romero, I., Segurado, J., 2019. Development of a thermo-mechanically coupled crystal plasticity modeling framework: application to polycrystalline homogenization. Int. J. Plast. 119, 313–330.
Li, H., Wang, Y., Zhang, C., Zhang, B., 2016. Effects of thermal histories on interfacial properties of carbon fiber/polyamide 6 composites: Thickness, modulus, adhesion and shear strength. Composites A 85, 31–39.
Lion, A., 1997. On the large deformation behaviour of reinforced rubber at different temperatures. J. Mech. Phys. Solids 45 (11–12), 1805–1834.
Lion, A., 1999. Strain-dependent dynamic properties of filled rubber: a non-linear viscoelastic approach based on structural variables. Rubber Chem. Technol. 72 (2), 410–429.
Lion, A., 2000. Constitutive modelling in finite thermoviscoplasticity: A physical approach based on nonlinear rheological models. Int. J. Plast. 16 (5), 469–494.
Lubliner, J., 1985. A model of rubber viscoelasticity. Mech. Res. Commun. 12 (2), 93–99.
Melro, A., Camanho, P., Pires, F.A., Pinho, S., 2013a. Micromechanical analysis of polymer composites reinforced by unidirectional fibres: Part II–micromechanical analyses. Int. J. Solids Struct. 50 (11-12), 1906–1915.
Melro, A., Camanho, P., Pires, F., Pinho, S., 2013b. Micromechanical analysis of polymer composites reinforced by unidirectional fibres: part i–constitutive modelling. Int. J. Solids Struct. 50 (11-12), 1897–1905.
Miehe, C., 2002. Strain-driven homogenization of inelastic microstructures and composites based on an incremental variational formulation. Int. J. Numer. Methods Eng. 55 (11), 1285–1322.
Naya, F., González, C., Lopes, C., Van der Veen, S., Pons, F., 2017. Computational micromechanics of the transverse and shear behavior of unidirectional fiber reinforced polymers including environmental effects. Composites A 92, 146–157.
Nguyen, V., Stroeven, M., Sluys, L., 2011. Multiscale continuous and discontinuous modeling of heterogeneous materials: a review on recent developments. J. Multiscale Model. 3 (04), 229–270.
Omairey, S., Dunning, P., Sriramula, S., 2019. Development of an ABAQUS plugin tool for periodic RVE homogenisation. Eng. Comput. 35, 567–577.
Özdemir, I., Brekelmans, W., Geers, M., 2007. Computational homogenization for heat conduction in heterogeneous solids. Int. J. Numer. Methods Eng. 73 (2), 185–204.
Özdemir, I., Brekelmans, W., Geers, M., 2008. Fe2 computational homogenization for the thermo-mechanical analysis of heterogeneous solids. Comput. Methods Appl. Mech. Engrg. 198 (3–4), 602–613.
Poggenpohl, L., Holthusen, H., Simon, J.-W., 2022a. Failure zone homogenization at mode II and mixed mode loading including gradient-extended damage and interface debonding at finite strains. Compos. Struct. 298, 115997.
Poggenpohl, L., Holthusen, H., Simon, J.-W., 2022b. Failure zone homogenization for modeling damage-and debonding-induced softening in composites including gradient-extended damage at finite strains. Int. J. Plast. 154, 103277.
Raju, K., Tay, T.-E., Tan, V., 2021. A review of the fe 2 method for composites. In: Multiscale and Multidisciplinary Modeling, Experiments and Design. Vol. 4, pp. 1–24.
Reese, S., Govindjee, S., 1998. A theory of finite viscoelasticity and numerical aspects. Int. J. Solids Struct. 35 (26–27), 3455–3482.
Reuvers, M., Kulkarni, S., Boes, B., Felder, S., Wutzler, A., Johlitz, M., Lion, A., Brepols, T., Reese, S., 2024. A thermo-mechanically coupled constitutive model for semi-crystalline polymers at finite strains: Mechanical and thermal characterization of polyamide 6 blends. Contin. Mech. Thermodyn. 36, 657–698.
Schmidt, A., Gierden, C., Waimann, J., Svendsen, B., Reese, S., 2023. Two-scale FE-FFT-based thermo-mechanically coupled modeling of elasto-viscoplastic polycrystalline materials at finite strains. PAMM 22 (1), e202200172.
Schneider, M., 2021. A review of nonlinear fft-based computational homogenization methods. Acta Mech. 232 (6), 2051–2100.
Schröder, J., 2014. A numerical two-scale homogenization scheme: the FE2-method. In: Plasticity and beyond: Microstructures, Crystal-Plasticity and Phase Transitions. Springer, pp. 1–64.
Segal, L., 1979. The thermal expansion of reinforced nylon-6 composites through the matrix glass transition temperature. Polym. Eng. Sci. 19 (5), 365–372.
Selmi, A., Doghri, I., Adam, L., 2011. Micromechanical simulations of biaxial yield, hardening and plastic flow in short glass fiber reinforced polyamide. Int. J. Mech. Sci. 53 (9), 696–706.
Shan, G.-F., Yang, W., Yang, M., Xie, B., Feng, J., Fu, Q., 2007. Effect of temperature and strain rate on the tensile deformation of polyamide 6. Polymer 48 (10), 2958–2968.
Sidoroff, F., 1974. Un modèle viscoélastique non linéaire avec configuration intermédiaire. J. Méc. 13, 679–713.
Spahn, J., Andrä, H., Kabel, M., Müller, R., 2014. A multiscale approach for modeling progressive damage of composite materials using fast fourier transforms. Comput. Methods Appl. Mech. Engrg. 268, 871–883.
Temizer, I., Wriggers, P., 2011. Homogenization in finite thermoelasticity. J. Mech. Phys. Solids 59 (2), 344–372.
Tian, W., Qi, L., Chao, X., Liang, J., Fu, M., 2019. Numerical evaluation on the effective thermal conductivity of the composites with discontinuous inclusions: Periodic boundary condition and its numerical algorithm. Int. J. Heat Mass Transfer 134, 735–751.
Tschoegl, N., 1971. Failure surfaces in principal stress space. In: Journal of Polymer Science Part C: Polymer Symposia. Vol. 32, Wiley Online Library, pp. 239–267.
Van der Sluis, O., Schreurs, P., Brekelmans, W., Meijer, H., 2000. Overall behaviour of heterogeneous elastoviscoplastic materials: effect of microstructural modelling. Mech. Mater. 32 (8), 449–462.
Vaughan, T., McCarthy, C., 2010. A combined experimental–numerical approach for generating statistically equivalent fibre distributions for high strength laminated composite materials. Compos. Sci. Technol. 70 (2), 291–297.
Wang, W., Dai, Y., Zhang, C., Gao, X., Zhao, M., 2016. Micromechanical modeling of fiber-reinforced composites with statistically equivalent random fiber distribution. Materials 9 (8), 624.
Wicht, D., Schneider, M., Böhlke, T., 2021. Computing the effective response of heterogeneous materials with thermomechanically coupled constituents by an implicit fast fourier transform-based approach. Internat. J. Numer. Methods Engrg. 122 (5), 1307–1332.
Xie, R., Weisen, A., Lee, Y., Aplan, M., Fenton, A., Masucci, A., Kempe, F., Sommer, M., Pester, C., Colby, R., et al., 2020. Glass transition temperature from the chemical structure of conjugated polymers. Nat. Commun. 11 (1), 893.